Conjugate natural heat transfer scrutiny in differentially heated cavity partitioned with a conducting solid using the lattice Boltzmann method

M. Ferhi[1,2] · R. Djebali[2] · S. Abboudi[3] · H. Kharroubi[4]

Abstract

In the present paper, we numerically investigated the two-dimensional conjugate heat transfer problems in a unitary computational domain containing both the solid and fluid regions. The physical problem configuration consists of two adiabatic horizontal walls of finite thickness and two vertical walls; the left one is maintained at hot temperature T_h and the right one is maintained at cold temperature T_c. The lattice Boltzmann method (LBM) based on the BGK model has been used to simulate laminar natural convection in the partitioned air-filled cavity with a heat-conducting solid. In the interface boundaries of the heat-conducting solid, the continuity of temperature and heat transfer is considered. A series of numerical simulation is carried out over a wide range of the Rayleigh number ($Ra=10^3$–10^6), the thermal conductivity ratio k_r and the solid partition thickness ($\delta=1$–95%) and its horizontal position. The results show that the partition reduces the heat transfer rate in the cavity. For a centered partition ($X_s=0.5$), the average Nusselt number decreases almost linearly with partition thickness for $\delta \leq 0.45$; however, it increases for $\delta \geq 0.45$ due to the confinement in the thin fluid regions. For $Ra=10^5$, the heat transfer rate decreases with the partition position until a critical value close to 0.325 and rises slightly until $X_s=0.5$. The critical position value decreases with the Ra number increase and it is close to 0.2 for $Ra=10^6$ where $Nu=3.766$. The heat transfer rate is enhanced with the increase in thermal conductivity. Correlations of the average Nusselt numbers are obtained as a function of Rayleigh number.

Keywords LBM · Conjugate natural convection · Partitioned cavity · Heat transfer · Nusselt number · Conducting solid

List of symbols

c	Lattice speed
c_s	Lattice speed of sound
c_i	Discrete particle speed
f	Density distribution functions
f^{eq}	ρ-equilibrium distribution functions
g	Temperature distribution functions
g^{eq}	θ-equilibrium distribution functions
ω_i	Weight factor
k_f	Fluid thermal conductivity (W m^{-1} K^{-1})
k_s	Solid thermal conductivity (W m^{-1} K^{-1})
k_r	Thermal conductivity ratio
m, n	Lattice cell numbers
Nu	Local Nusselt number $=\partial\theta/\partial X$
$\overline{Nu}$	Average Nusselt number $= \int_{Y=0}^{1} Nu\, dY$
p	Pressure (Pa)
Ra	Rayleigh number $=Ra=g\beta(T_h-T_c)W^3/\alpha\upsilon$
Pr	Prandtl number $=\upsilon/\alpha$
T	Temperature (K)
T_c	Temperature of the cold wall (K)
T_h	Temperature of the hot wall (K)
u, v	Dimensional velocities (m s^{-1})
U, V	Non-dimensional velocities
H	Height of the cavity (m)
W	Width of the cavity (m)
x, y	Coordinates system (–)
X, Y	Non-dimensional Cartesian coordinates

✉ M. Ferhi
moktar.ferhi@gmail.com

1 Higher National Engineering School of Tunis, University of Tunis, 5 Avenue Taha Hussein, 1008 Tunis, Tunisia

2 LR: Subatomic Physics, Nanoscience and Energetics, IPEST, La Marsa, University of Carthage, Tunis 2070, Tunisia

3 ICB, UMR 6303, CNRS, Université de Bourgogne Franche-Comté, UTBM Département COMM, 90010 Belfort, France

4 UR: Renewable Energy for Agriculture and Agro-Industry, ESIM, University of Jendouba, Jendouba, Tunisia

X_s Position of the partition
t Time (s)

Greek symbols

α Thermal diffusivity ($m^2\ s^{-1}$)
β Coefficient of thermal expansion (K^{-1})
Δx Lattice spacing
Δt Time increment (s)
μ Dynamic viscosity ($kg\ m^{-1}\ s^{-1}$)
ρ Fluid density ($kg\ m^{-3}$)
τ_α Relaxation time for temperature ($m^2\ s^{-1}$)
τ_υ Relaxation time for flow ($m^2\ s^{-1}$)
θ Non-dimensional temperature
υ Kinematic viscosity ($m^2\ s^{-1}$)
δ Thickness of the conducting body (m)
τ Dimensionless time

Subscript

c   Cold surface
f   Fluid
h   Hot surface
s   Solid

Introduction

Solid–fluid conjugate heat transfer (CHT) is commonly used in heat transfer in engineering devices, such as heat exchangers, combustion chambers, cooling of electronic devices, electronic equipment [1–3], the heat transport in microfuel cells and microchannels [4, 5]. In this context, many research topics have been published. In the area of industrial automobile, Ali et al. [6, 7] investigated experimentally the heat transfer inside a car radiator using metal oxide nanofluid. The use of nano-suspensions increases the heat transfer rate comparing with the water base fluid. The increase in the volume concentration enhances the heat transfer. The heat transfer rates are weakly dependent on the inlet nanofluid temperature.

Besides, numerical simulations of CHT problems are performed by many researchers using conventional numerical methods for solving the governing Navier–Stokes and energy equations. Finite volume method (FVM), finite difference method (FDM), and finite element method (FEM) have been successfully applied [8–10]. However, different material properties at solid–fluid interface caused some difficulties in simulation of heat transfer [11, 12]. In addition, the implementation of conjugate interface thermal boundary conditions is a challenging problem, particularly for complex geometries.

Moreover, with the growth of the capacity of computer machines, new numerical methods are emerging. This is typically the so-called lattice Boltzmann-type methods

known by the acronym LBM or its ancestor lattice gas automata (LGA). Based on the evolution of particle distribution functions of discrete velocities, the LBM method with its four models (BGK, MRT, entropic and regularized LBM) has been developed rapidly in recent years and has received much attention in science and engineering as a powerful computational tool for solving a large class of problems. The LBM has been successfully used to solve a wide range of thermo-fluid problems [13–16]. LBM is based on mesoscopic scale, which has many advantages over conventional computational fluid dynamics (CFD) solvers.

Lu et al. [17] proposed FD-LBM in order to simulate CHT problems, in which the continuity of heat flux at the interface between two different media was obtained by modifying the streaming process to avoid exchanging information directly between different media because the conventional streaming process cannot keep heat flux continuous at the interface in CHT. The distribution functions at the interface can be obtained by coupling the interface conditions of temperature and heat flux with non-equilibrium extrapolation. Authors tested four cases and showed that simple difference method based on the coupling between two distribution functions has a good performance in simulating solid–fluid or solid–solid CHT problems. A promising difference method was proposed by Mohamad et al. [18]. The continuity of heat flux at the interface was ensured by coupling temperature difference with a new scaling law of energy distribution function. Koca et al. [19] used the Bejans' heatline technique to analyze the effects of a differentially thickness change conductive partition on natural convection heat transfer in an enclosure. It was found that both heat transfer and flow strength strongly depend on the thermal conductivity ratio and Rayleigh number.

Karani and Huber [20] suggested using a source term to the evolution equation in such a way that temperature and heat flux continuities were satisfied at the interface. In their method, the interface was placed halfway between the boundary lattice nodes.

Benachour et al. [21] made a series of numerical simulations to develop a new correlation using the Lagrange polynomial interpolation method for high Rayleigh numbers. This method is used for predicting exchange coefficient and estimating Nusselt number to optimize the design of walls in buildings. Authors found that the heat transfer decreases with the increase in the wall thickness of the building material of the outer wall. The Nusselt number increases when the Rayleigh number increases.

Khatamifar et al. [22] made a series of numerical simulation for conjugate natural convection flow and heat transfer using the finite volume method in a partitioned differentially heated square cavity. They examined the effects of partition position and thickness on the unsteady

conjugate natural convection heat transfer in a differentially heated partitioned enclosure over a wide range of Rayleigh numbers. The presence of the heat-conducting solid has significant effects on heat and flow characteristics in the cavity. In addition, the average Nusselt number is a decreasing function of partition thickness but is an increasing function of the Rayleigh number. Finally, the position of the heat-conducting solid has a negligible influence on the heat transfer rate for the whole range of Rayleigh number considered.

The numerical results of Ho and Yih [23] show that heat transfer in an air-filled partitioned rectangular cavity is considerably lower than that in a non-partitioned cavity. Indeed, the presence of a conducting partition in the cavity has a significant influence on the natural convection heat transfer characteristics across the cavity.

Saeid [24] used the finite volume method to simulate conjugate natural convection in two-dimensional vertical porous layer sandwiched between two equal-thickness walls. The numerical results indicated that the ratio of the wall thickness to its height, the wall to porous thermal conductivity ratio and the Rayleigh number have great effects on the heat transfer and fluid flow characteristics. It was found that as the average Nusselt number decreases the wall thickness increases. The strength of the circulation is much higher with thin walls and with high thermal conductivity ratio. The numerical results indicated that for small values of Rayleigh number, the average Nusselt number is approximately constant.

The earlier research in this area has been conducted by Wang et al. [25]. Authors proposed a CFD model for simulating the CHT at the fluid–solid interface using the LB method. The half-lattice technique was employed to model the interface. The model has given reasonable results for steady-state heat conduction problems.

A finite difference approach has been proposed by Seddiq et al. [26] to deal with the CHT problems, in which the continuous heat flux at the interface between two different media can be well guaranteed. However, this method is confined to solids with a square shape at steady state.

Souayeh et al. [27] investigated numerically the steady laminar natural convection in a water-filled 2D enclosure containing a rectangular conducting body. To study the impact on the flow structure and heat transfer characteristics, several parameters are highlighted such as Rayleigh number, solid–fluid thermal conductivity ratio and different locations of a conducting body. It was found that the location of the rectangular conducting body affects only the flow structure and has no effect on temperature field. By increasing the Rayleigh number, the gradient of thermal boundary layer becomes larger. As a consequence, the heat transfer rate increases. A comparative study was made between the two cases, vertical and horizontal location of

the conducting bloc. It is found that the mean Nusselt number is higher for vertically positioned case.

Ben Nakhi and Chamkha [28] made a numerical investigation in which they studied the influence of length and inclination angle of heated thin fin attached in the hot wall of a differentially heated cavity. The FVM is used to obtain the numerical solution. They found that the considered parameters have a significant effect on the heat transfer. Besides, the heat transfers decrease when the length of the hot fin increases. Depending on the thin fin length, the behavior of the average Nusselt number changes when the inclination angle increases. In addition, the increase in Rayleigh numbers produces a significant augmentation in heat transfer. In fact, as well as the Rayleigh number, it is possible to enhance or reduce wall heat transfer by proper selection of both fin inclination angle and length. In another study, Ben Nakhi and Chamkha [29] studied numerically the CHT in a square cavity which has three thick-cooled thick walls and one thin-heated vertical wall with a heated inclined thin fin attached to its middle. They found that the thin fin inclination angle, length and the solid–fluid thermal conductivity ratio have a significant influence on the heat transfer rate. Besides, the control of the behavior of heat transfer through an enclosure is done by means of the selected parameters.

Ismael and Chamkha [30] investigate numerically the conjugate natural convection in a differentially square composite vertically layered cavity using the FDM. The cavity is subdivided from the left: a solid wall, a porous layer, and a nanofluid layer. It was found that, at low value of the porous medium permeability and when the porous layer thickness is greater than 0.5, the natural convection heat transfer was enhanced when the Rayleigh number is less than or equal to 10^4. The solid wall type is found to play a considerable role in the flow and heat transfer fields. It is also found that the conduction heat transfer within the solid wall is affected by the permeability of the porous layer.

Chamkha et al. [31] conducted a numerical study of mixed convection heat transfer in a heated square solid cylinder located at the center of a vented cavity filled with air. The FDM is used to solve the considering equations. They found that the heat transfer increases linearly with the Richardson number for all considered configurations. As the Richardson and Reynolds numbers increase, the heat transfer along the hot wall increases while the surface temperature decreases for the same parameters for all configurations. The authors found that, in terms of heat transfer, the performance of the CT configuration is more pronounced than the CC and CB configurations. The position of the inner square cylinder has an important role in the streamline and isotherm contour patterns.

Chamkha [32] performed a numerical study of CHT in porous cavity heated by triangular thick wall using the second-order central differences finite difference scheme with the successive over relaxation (SOR) method. It was found that the heat transfer and the circulation strength are the increasing functions with Rayleigh numbers. The increase in the solid wall thickness causes at the same time the augmentation of thermal resistance and increases the contact interface. When the thermal conductivity ratio is less than 0.1, the effect of Ra and D become more pronounced.

Chamkha and Ismael [33] made a numerical investigation of natural convection in a differentially heated and partially cavity filled with nanofluid. The obtained results show that the heat transfer is an increasing function of Ra at lower porous layer thicknesses. The use of nanofluid enhances the convective heat transfer, precisely at low permeability porous layer. It was found that the addition of the nanofluid accelerates the flow throughout the cavity. The convective heat transfer presents a maximum value corresponding to a critical porous layer thickness for a considered effective thermal conductivity. The aspect ratio $A = 2$ corresponds to the best value of convective heat transfer.

Ismael et al. [34] considered the case of Chamkha et al. [32], but they focus on the irreversibility of heat transfer and fluid friction process. The authors conclude that the considered nanofluid increases the global entropy generation. The global entropy generation rate is an increase function of conductivity solid wall. For low Ra, the rate of entropy generation increases with solid wall thickness for highly conductive wall. On the other hand, for high Ra, the maximum of heat transfer corresponds to a critical value of $D = 0.7$ for conductive solid wall less than 1 and the maximum irreversibility appears at $D = 0.5$.

The objective of the present contribution is to simulate laminar natural convection in a two-dimensional square cavity partitioned with a conducting solid.

The remainder of this paper is organized as follows: The section two is devoted to the numerical modeling where the mathematical formulation, boundary conditions and the LBM basis are presented. In the third section, the independence test and the code validation are performed. The fourth section is concerned with the results and discussion where the effect of the partition wall, the effect of wall thickness, the effects of partition position and Rayleigh number, the effect of thermal conductivity ratio on the dynamic and thermal structures and heat transfer rate measured using the Nusselt number are appraised. Concluding remarks are finally drawn in "Conclusions" section.

Numerical modeling

Problem statement

The geometry of the problem is shown in Fig. 1. It displays a two-dimensional partitioned square enclosure. In this configuration, the horizontal walls are adiabatic, while the vertical ones are maintained at constant but different temperatures so that the cavity is heated from the right vertical wall and cooled from the opposite left vertical one. A heat-conducting solid partition is placed in the cavity. All the walls are rigid, and no-slip BC is considered. The partition walls are heat conducting, with finite thermal conductivity k_s [22]. The fluid flow is assumed to be laminar and incompressible, and the Boussinesq approximation is adopted for the variations of the density in the buoyancy term.

Mathematical formulation and boundary conditions

The equations governing the dynamic and thermal fields are the Navier–Stokes coupled with the energy equations, given as follows:

Continuity equation:

$$\frac{\partial u}{\partial x} + \frac{\partial v}{\partial y} = 0 \tag{1}$$

Momentum equations:

$$\frac{\partial u}{\partial t} + u\frac{\partial u}{\partial x} + v\frac{\partial u}{\partial y} = -\frac{1}{\rho}\frac{\partial p^*}{\partial x} + v\left(\frac{\partial^2 u}{\partial x^2} + \frac{\partial^2 u}{\partial y^2}\right) \tag{2}$$
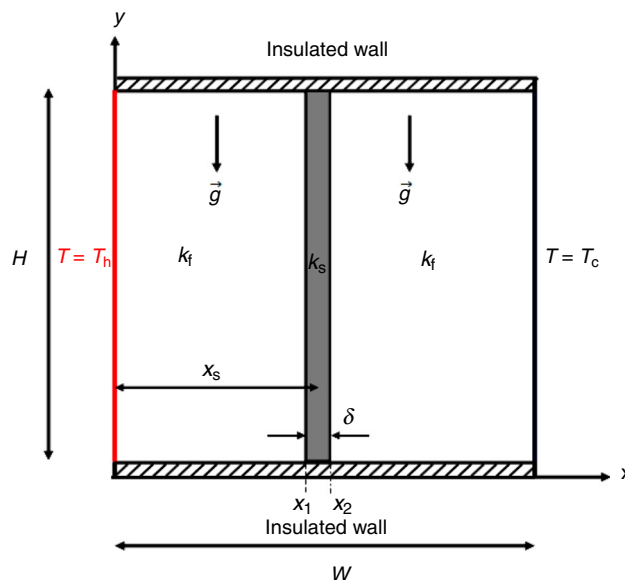

Fig. 1 Physical domain and coordinate system

$$\frac{\partial v}{\partial t} + u\frac{\partial v}{\partial x} + v\frac{\partial v}{\partial y} = -\frac{1}{\rho}\frac{\partial p^*}{\partial y} + \upsilon\left(\frac{\partial^2 v}{\partial x^2} + \frac{\partial^2 v}{\partial y^2}\right) + g\beta(T_f - T_c) \tag{3}$$

Energy equation for the fluid:

$$\frac{\partial T_f}{\partial t} + u\frac{\partial T_f}{\partial x} + v\frac{\partial T_f}{\partial y} = \alpha\left(\frac{\partial^2 T_f}{\partial x^2} + \frac{\partial^2 T_f}{\partial y^2}\right) \tag{4}$$

Energy equation for the solid:

$$\frac{\partial^2 T_s}{\partial x^2} + \frac{\partial^2 T_s}{\partial y^2} = 0 \tag{5}$$

where $p^* = p + \rho g y$ and p is the relative pressure.

Where T_c is the temperature of the right vertical wall of the cavity.

The following non-dimensional variables are introduced to proceed with the numerical solution of the above-mentioned equations:

$$X = \frac{x}{W}, \quad Y = \frac{y}{W}, \quad U = \frac{uW}{\alpha}, \quad V = \frac{vW}{\alpha}, p = \frac{p^*W^2}{\rho\alpha^2},$$
$$\theta = \frac{T - T_c}{T_h - T_c}, \quad Ra = \frac{g\beta(T_h - T_c)W^3}{\alpha\upsilon}, \quad \tau = \frac{t\alpha}{W^2},$$
$$Pr = \frac{\upsilon}{\alpha}$$

The non-dimensionalized continuity, momentum and energy equations can be expressed as:

$$\frac{\partial U}{\partial X} + \frac{\partial V}{\partial Y} = 0 \tag{6}$$

$$\frac{\partial U}{\partial \tau} + U\frac{\partial U}{\partial X} + V\frac{\partial U}{\partial Y} = -\frac{\partial P}{\partial X} + Pr\left(\frac{\partial^2 U}{\partial X^2} + \frac{\partial^2 U}{\partial Y^2}\right) \tag{7}$$

$$\frac{\partial V}{\partial \tau} + U\frac{\partial V}{\partial X} + V\frac{\partial V}{\partial Y} = -\frac{\partial P}{\partial Y} + Pr\left(\frac{\partial^2 V}{\partial X^2} + \frac{\partial^2 V}{\partial Y^2}\right) + RaPr\theta \tag{8}$$

$$\frac{\partial \theta_f}{\partial \tau} + U\frac{\partial \theta_f}{\partial X} + V\frac{\partial \theta_f}{\partial Y} = \frac{\partial^2 \theta_f}{\partial X^2} + \frac{\partial^2 \theta_f}{\partial Y^2} \tag{9}$$

$$\frac{\partial^2 \theta_s}{\partial X^2} + \frac{\partial^2 \theta_s}{\partial Y^2} = 0 \tag{10}$$

The non-dimensional boundary conditions are defined as follows:

$$\begin{cases} U = V = 0 & \text{at } X = 0, W \quad \text{and} \quad Y = 0, W \\ \theta = 1 & \text{at } X = 0 \quad \text{and} \quad \theta = 0 \text{ at } X = W \\ \frac{\partial \theta}{\partial Y} = 0 & \text{at } Y = 0, W \\ \left(\frac{\partial \theta}{\partial X}\right)_{\text{fluid}} = k_r\left(\frac{\partial \theta}{\partial X}\right)_{\text{solid}} & \text{at } X = X_1, X_2 \end{cases} \tag{11}$$

where the thermal conductivity ratio is defined as $k_r = k_s/k_f$.

The local Nusselt number evaluating the heat transfer rate at the active vertical walls is defined as follows:

$$Nu_{\text{local}} = \frac{\partial \theta}{\partial X} \tag{12}$$

The average Nusselt number $\overline{Nu}$ is defined as follows:

$$\overline{Nu} = \int_0^1 Nu_{\text{local}} \, dY = \sum_0^n Nu_i \tag{13}$$

Lattice Boltzmann method basis

The lattice Boltzmann equation (LBE) was originated from Ludwig Boltzmann's kinetic theory of gases. It explains and predicts how the properties of atoms and molecules (microscopic properties) determine the phenomenological (macroscopic) properties of matter. The distribution function (probability of finding particles within a certain range of velocities at a certain range of locations at a given time) replaces tagging each particle, as in molecular dynamic simulations.

Flow and temperature fields

The distribution functions are calculated by solving the LBE, which is a special discretization of the kinetic Boltzmann equation:

$$\frac{\partial f_k}{\partial t} + c_k\nabla f_k = \frac{\Delta t}{\tau_\upsilon}\left(f_k^{eq} - f_k\right) \tag{14}$$

After introducing Bhatnagar–Gross–Krook (BGK) [35] approximation, the Boltzmann equation was reformulated consisting of two steps: collide and stream. The collision step is defined as follows:

$$f_k(x + c_k\Delta t, t + \Delta t) = f_k(x, t) + \frac{\Delta t}{\tau_\upsilon}\left[f_k^{eq}(x, t) - f_k(x, t)\right] \tag{15}$$

The streaming step represents the advection of the fluid particles. This can be written as:

$$f_k(x + c_k\Delta t, t + \Delta t) = f_k(x, t + \Delta t) \tag{16}$$

The exchange of momentum and energy is achieved through particles collision and streaming. For non-isothermal problems, the LBM utilizes generally two distribution functions f and g, for the flow and temperature fields, respectively. In this study, the temperature field is simulated by D2Q9 new distribution function g_i. The corresponding LBE without source/sink term is:

$$g_k(x + c_k\Delta t, t + \Delta t) = g_k(x, t) + \frac{\Delta t}{\tau_\alpha}\left[g_k^{eq}(x, t) - g_k(x, t)\right] \tag{17}$$

The present study examines two-dimensional problem by square lattice with nine velocities (D2Q9 model). The velocity vectors of the D2Q9 model are shown in Fig. 2. For the D2Q9 model, the discrete velocities set c_k are written as:

$$c_k = \begin{pmatrix} c_{kx} \\ c_{ky} \end{pmatrix} = \begin{pmatrix} 0 & 1 & 0 & -1 & 0 & 1 & -1 & -1 & 1 \\ 0 & 0 & 1 & 0 & -1 & 1 & 1 & -1 & -1 \end{pmatrix} \quad (18)$$

The distribution functions for the next time step are then computed with the post-streaming distribution functions and the equilibrium distribution functions. For the D2Q9 model, f^{eq} and g^{eq} are given by the following:

$$f_k^{eq} = \rho \omega_k \left[1 + 3\frac{c_k.u_i}{c^2} + \frac{9(c_k.u_i)^2}{2c^4} - \frac{3u_i^2}{2c^2} \right] \quad (19)$$

$$g_k^{eq} = \theta \omega_k \left[1 + 3\frac{c_k.u_i}{c^2} \right] \quad (20)$$

For simulation of heat transfer in the solid part, equilibrium distribution function is as follows:

$$g_k^{eq} = \theta \omega_k \quad (21)$$

where the values of ω_k are as follows:

$$\omega_0 = 4/9, \quad \omega_{k=1-4} = 1/9, \quad \omega_{k=5-8} = 1/36 \quad (22)$$

The LB method is nowadays a powerful numerical technique, based on kinetic theory, for simulating fluid flow and heat transfer [36–40], and has many advantages in comparison with conventional CFD methods mentioned previously.

The dynamic and thermal macroscopic quantities are computed as:

$$\rho(x, t) = \sum_{k=0}^{8} f_k \quad (23)$$

$$\rho(x, t)u_i(x, t) = \sum_{k=0}^{8} c_k f_k \quad (24)$$

$$\theta(x, t) = \sum_{k=0}^{8} g_k \quad (25)$$

where the kinematic viscosity υ and the thermal diffusivity α are related to the flow and heat relaxation times as follows:

$$\upsilon = \left[\tau_\upsilon - \frac{1}{2} \right] c_s^2 \Delta t \quad \alpha = \left[\tau_\alpha - \frac{1}{2} \right] c_s^2 \Delta t \quad (26)$$

where c_s is the lattice speed of sound and equals $c_s^2 = c/3$.

LBM boundary conditions treatment for fluid flow

One of the important and crucial issues in LBM simulation of flow and temperature is accurate implementation of the boundary conditions. Therefore, we need to determine appropriate equations for calculating those distribution functions f and g, for the flow and temperature at the boundaries for a given physical condition. The domain is divided into $(n+1) \times (m+1)$ nodes with $n=m$, so n^2 square cells and will be confound in the following the node (x_i, y_i) and (i, j).

The incoming unknown distribution functions pointing to the fluid zone at boundary nodes must be specified. For the no-slip boundary condition, bounce-back boundary condition is applied on all solid boundaries. This means that incoming distribution functions are equal to outgoing ones after the collision [41]. For instance, for the east boundary, the following conditions are imposed:

Fig. 2 Flow domain discretization using the D2Q9 model (left) and the nine-speed square lattice of the D2Q9 model (right)

$\Delta x = \Delta y = 1$
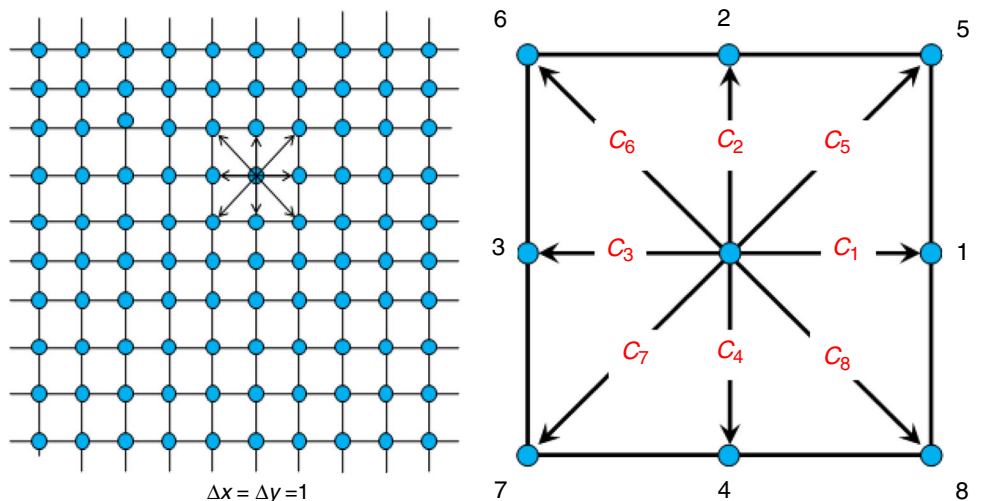
$$f_6(n,j) = f_8(n,j), \quad f_7(n,j) = f_5(n,j), \quad f_3(n,j) = f_1(n,j) \tag{27}$$

LBM boundaries treatment of temperature field

Bounce-back boundary condition (adiabatic) is used on the north and the south boundaries. For instance, for the north boundary, the following conditions are imposed.

$$g_7(i,m) = g_7(i,m-1), \quad g_8(i,m) = g_8(i,m-1), \quad g_8(i,m) = g_8(i,m-1) \tag{28}$$

The temperature at east and west walls is known, $\theta=1$ and $\theta=0$, respectively. Since we are using D2Q9, the unknowns for the west wall are g_1, g_5, g_8 which are evaluated as:

$$\begin{cases} g_1(0,j) = \theta_h(\omega(1) + \omega(3)) - g_3(0,j) \\ g_5(0,j) = \theta_h(\omega(5) + \omega(7)) - g_7(0,j) \\ g_8(0,j) = \theta_h(\omega(8) + \omega(6)) - g_6(0,j) \end{cases} \tag{29}$$

The unknowns for the east wall are g_3, g_6, g_7 which are evaluated as:

$$g_3(n,j) = -g_1(n,j), \quad g_6(n,j) = -g_8(n,j), \quad g_7(n,j) = -g_5(n,j) \tag{30}$$

LBM conjugate heat transfer treatment

In the present model, the temperature and the heat flux at the interface can be kept continuous naturally. Solving the last line of Eq. (11) for the temperature at the interface leads to:

At $X=X_1$

$$\theta(i,j) = \frac{\theta_f(i-1,j) + k_r \times \theta_s(i+1,j)}{1 + k_r} \tag{31}$$

At $X=X_2$

$$\theta(i,j) = \frac{k_r \times \theta_s(i-1,j) + \theta_f(i+1,j)}{1 + k_r} \tag{32}$$

Grid independence test and code validation

Enclosure without partition

The results presented in Table 1 show the maximum stream function magnitude and the average Nusselt number $\overline{Nu}$ variations with different grid sizes for an enclosure without partition wall. For $Ra=10^5$, we notice the convergence of the two physical quantities by increasing the mesh resolution. For the grid mesh 200×200 and 250×250, the

Table 1 Average Nusselt numbers obtained with different grid meshes for $Ra=10^5$

Grid mesh	50×50	100×100	150×150	200×200	250×250
$\overline{Nu}$	4.382	4.495	4.516	4.522	4.524
$|\psi|_{max}$	10.505	9.826	9.710	9.669	9.649

change of the Nusselt number holds in the third and the change of the $|\psi|_{max}$ does not exceed 0.2%. We adopt 200×200 number of grid as sufficient to obtain the accurate results for the present problem for $Ra \leq 10^5$.

The choice of this grid is confirmed by the horizontal velocity at the mid-width, the vertical velocity at the mid-height of the cavity and the temperature profile at the mid-width. To test the grid independence, numerical simulations were performed as shown in Fig. 3 for $Ra=10^5$ using different numbers of grid. We notice that the horizontal velocity, the vertical velocity and the temperature profile are similar for fairly large meshes.

In the following, we will adopt the grid resolutions 100^2 for $Ra=10^3$ and $Ra=10^4$, 200^2 for $Ra=10^5$ and 250^2 for $Ra=10^6$. Table 2 shows a comparison of the average Nusselt numbers obtained with the present code and those available in the literature for a differentially heated cavity at different Rayleigh numbers. From this table, we noticed that the obtained results show a good agreement with the last findings. The deviation of the mean Nusselt number according to numerical studies does not exceed 1.35% for all Rayleigh numbers. The maximum deviation according to the experimental study carried out by Baïri [42] is 6.59%.

Enclosure with partition

A second test case of our model for the differentially heated cavity with CHT was performed in comparison with the present FE COMSOL results [52] for $k_r=6.22$ and $Ra=10^5$. The temperature profiles and the local Nusselt number of the hot wall are depicted in Fig. 4. The results show an excellent agreement. The present and the COMSOL Nusselt numbers are 2.139 and 2.1142, respectively, thus a deviation close to 1.173%.

In order to test the effect of the grid mesh, we used the vertical velocity profile at the mid-height of the cavity for different numbers of grid (Fig. 5). This figure shows us that the velocity is the same even for fairly large meshes.

The two used test cases with and without partition show the high correctness and credibility of the present code. The emerging results were compared with well-chosen high-resolution schemes of the FV, FE, FD and LB methods as well as experimental measurements, and an

(a)

(b)

(c)
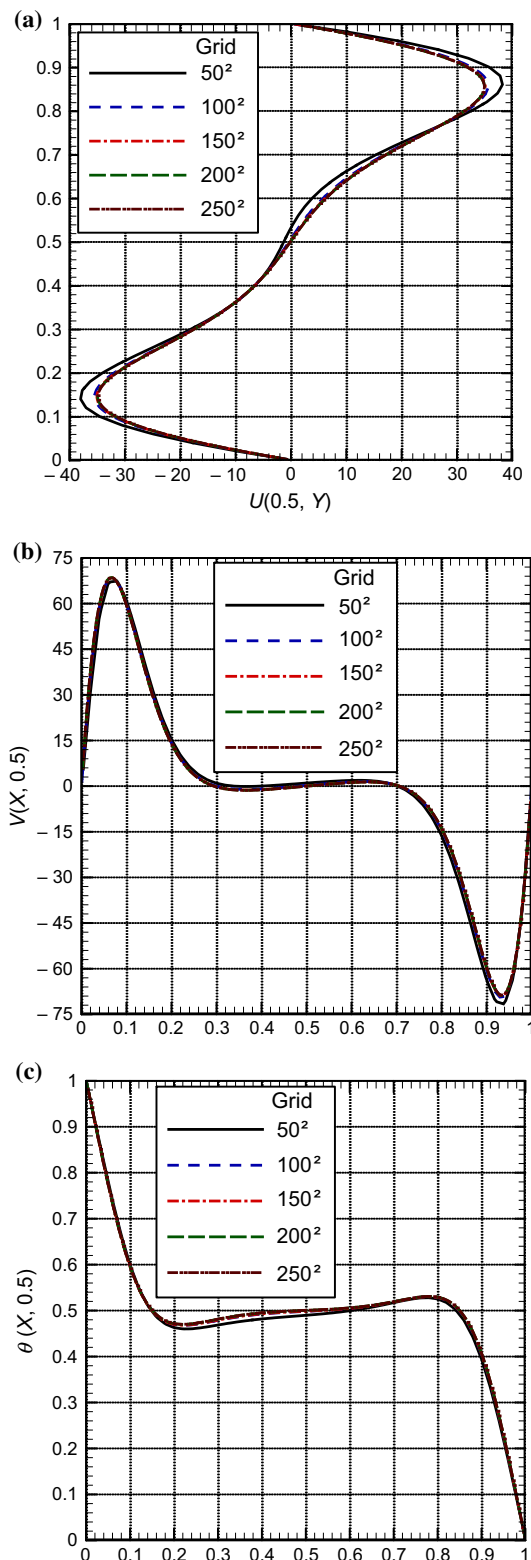
Fig. 3 Horizontal velocity profile $U(0.5, Y)$ (**a**), vertical velocity profile $V(X, 0.5)$ (**b**), and temperature profile $\theta(X, 0.5)$ for different grid meshes

excellent agreement was obtained. The present code and grid resolution will be used in the following to analyze and discuss the convective flow and heat transfer inside partitioned square cavity.

Results and discussion

Numerical simulations are carried out for natural convection CHT for partitioned cavity. As mentioned above, the governing parameters are the thickness of the conducting body, Rayleigh numbers and thermal conductivity ratio. The results are shown in terms of streamlines, isotherms, the average and local Nusselt numbers. The air is chosen as a working fluid having $Pr = 0.71$.

Effect of the partition wall on heat transfer rate

The aim of this part is to compare the heat transfer in the two cases with and without conducting wall for Rayleigh numbers ($10^3 \leq Ra \leq 10^6$). Figure 6 shows that the conducting partition has a significant influence on the heat transfer intensity at the active wall. The heat transfer rate is considerably reduced in the case of partitioned cavity. By analyzing the figure, it is noticed that the local Nusselt number decreases at the active wall for all Rayleigh numbers.

The impact of the partition wall on the rate of heat transfer for different Rayleigh numbers is presented in Fig. 7. The figure shows that the average Nusselt number of the cavity with CHT is lower than that without partition wall. The Rayleigh number has a great influence on the augmentation of heat transfer in the cavity. Heat exchange in the cavity increases with the increase in Rayleigh number due to the augmentation of the heat intensity. By introducing the conducting partition wall, we observe that the Nusselt number value undergoes a substantial reduction. In the case with partition, the block plays a damping rule countering the convective currents inside the cavity by altering the dynamic behavior and enhancing the confinement and buoyancy stability.

Effect of wall thickness

The wall thickness effect on the flow structure and isotherms is depicted in Fig. 8 for $k_r = 6.22$ and $Ra = 10^5$. It is observed that the thickness of partition does not have an important effect on the streamlines structure. As seen from the figure, two circulation cells are formed in each part of the enclosure and the flow structure are generally centrosymmetric. By increasing the thickness of the conducting body, the size of the formed circulation cells decreases and the streamlines become very tight. Both formed

Table 2 Comparison of the present and literature results at different Rayleigh numbers

Reference	Approach	Rayleigh numbers Ra			
		10^3	10^4	10^5	10^6
Present grid size		100^2	100^2	200^2	250^2
Present study	LBM	1.127	2.256	4.522	8.825
Djebali et al. [43]	LBM	1.115	2.226	4.508	8.713
Dixit and Babu [45]	LBM	1.118	2.256	4.519	8.817
Kuznik et al. [48]	LBM	1.117	2.246	2.518	8.792
Khatamifar et al. [22]	FVM	1.117	2.244	4.521	8.825
Moumni et al. [49]	FVM	1.117	2.244	2.521	8.824
Hortman et al. [50]	FVM	–	2.244	4.521	8.825
De Vahl Davis [44]	FDM	1.118	2.243	4.519	8.799
Khanafer et al. [46]	FDM	1.118	2.245	4.522	8.826
Mobedi [47]	FDM	1.117	2.240	2.510	8.803
Kalita et al. [51]	Fourth-order FDM	1.118	2.245	2.522	8.829
Baïri [42]	Exp.	1.112	2.168	4.228	8.243
Max dev. from num. (%)		1.08	1.35	0.31	1.29
Dev. from exp. study (%)		1.33	3.77	6.5	6.59
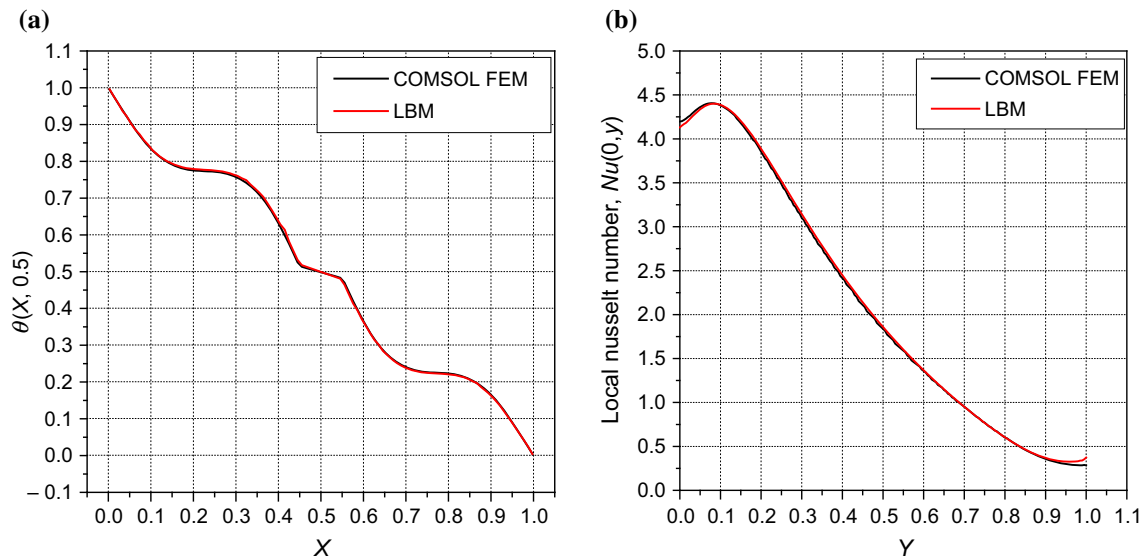
Fig. 4 Temperature profile $\theta(X, 0.5)$ (**a**) and the local Nusselt number (**b**) compared with those obtained by COMSOL

circulations rotate in a clockwise direction. As the wall thickness increases, the strength of the circulation within the cavity decreases and the absolute value of ψ decreases by increasing the wall thickness. As an example, $|\psi|_{max}=$ 6.264, 3.022 and 0. 0013 for, respectively, a wall thickness $\delta=0.1$, 0.4 and 0.95.

For a wall thickness tending to the unity, the pressure inside each part of the enclosure increases because the distance between the active wall and the partition decreases. The confinement of the flow induces a strong dynamic and thermal coupling between the different boundaries of the enclosure.

Figure 9 shows the isotherms at different values of conducting body thickness. It can be seen clearly from that, by increasing the thickness value δ of the partition wall, the isotherms become parallel to both sides of the conducting body and active walls. For $\delta \leq 0.5$, the temperature field undergoes a deviation in the solid–fluid interface. For $\delta > 0.5$, the isotherms become strictly parallel in the entire of the cavity. Obviously, as the wall thickness increases, the heat transfer mechanism changes from convection-dominant regime to conduction-dominant regime. By increasing the wall thickness δ, the intensity the temperature gradient becomes low and the convective motion is more dumped. This is more expressed at mid-height: the horizontal
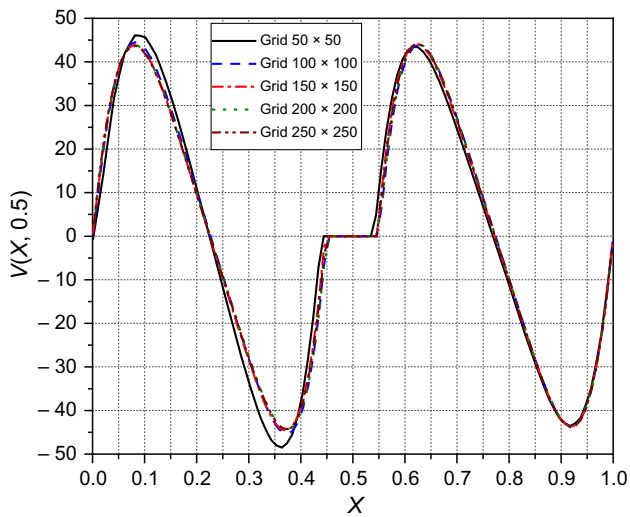
Fig. 5 Vertical velocity profile $V(X, 0.5)$ at different grid meshes for conjugate heat transfer
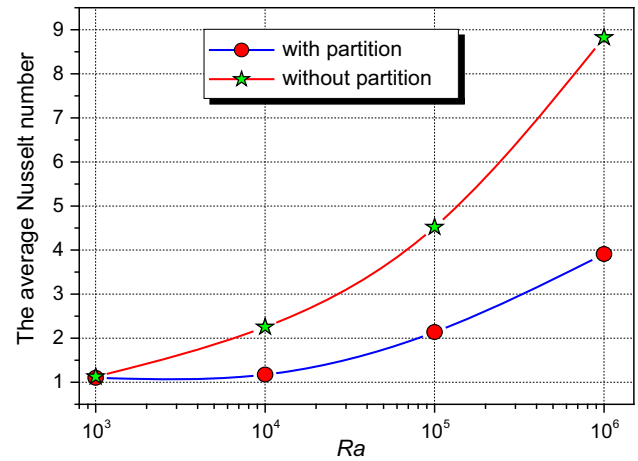

Fig. 7 Variation of the average Nusselt number at different Rayleigh numbers for a cavity with and without conducting wall for k_r=6.22, δ=0.1
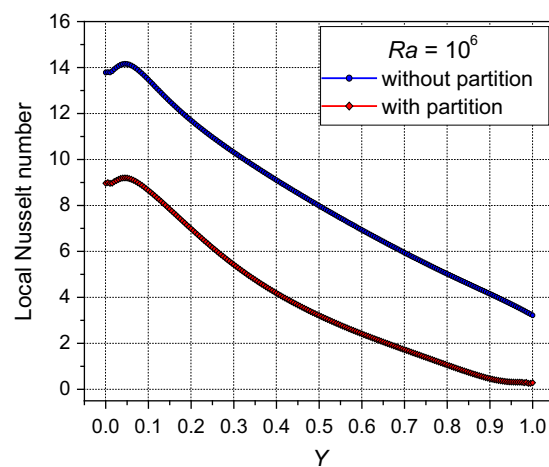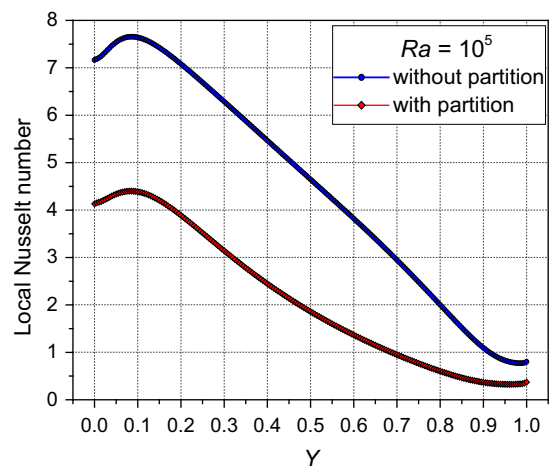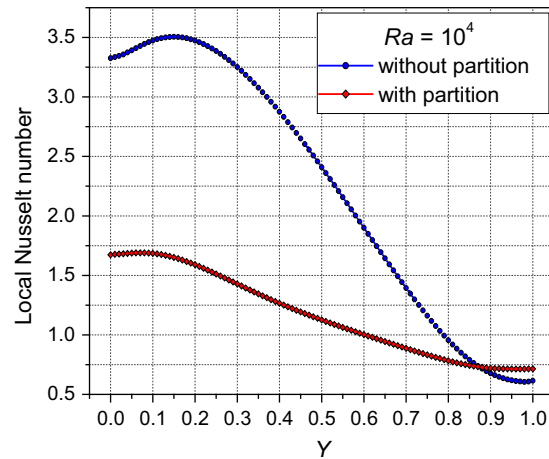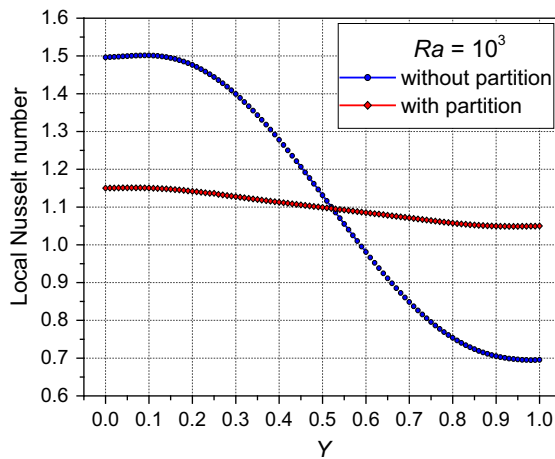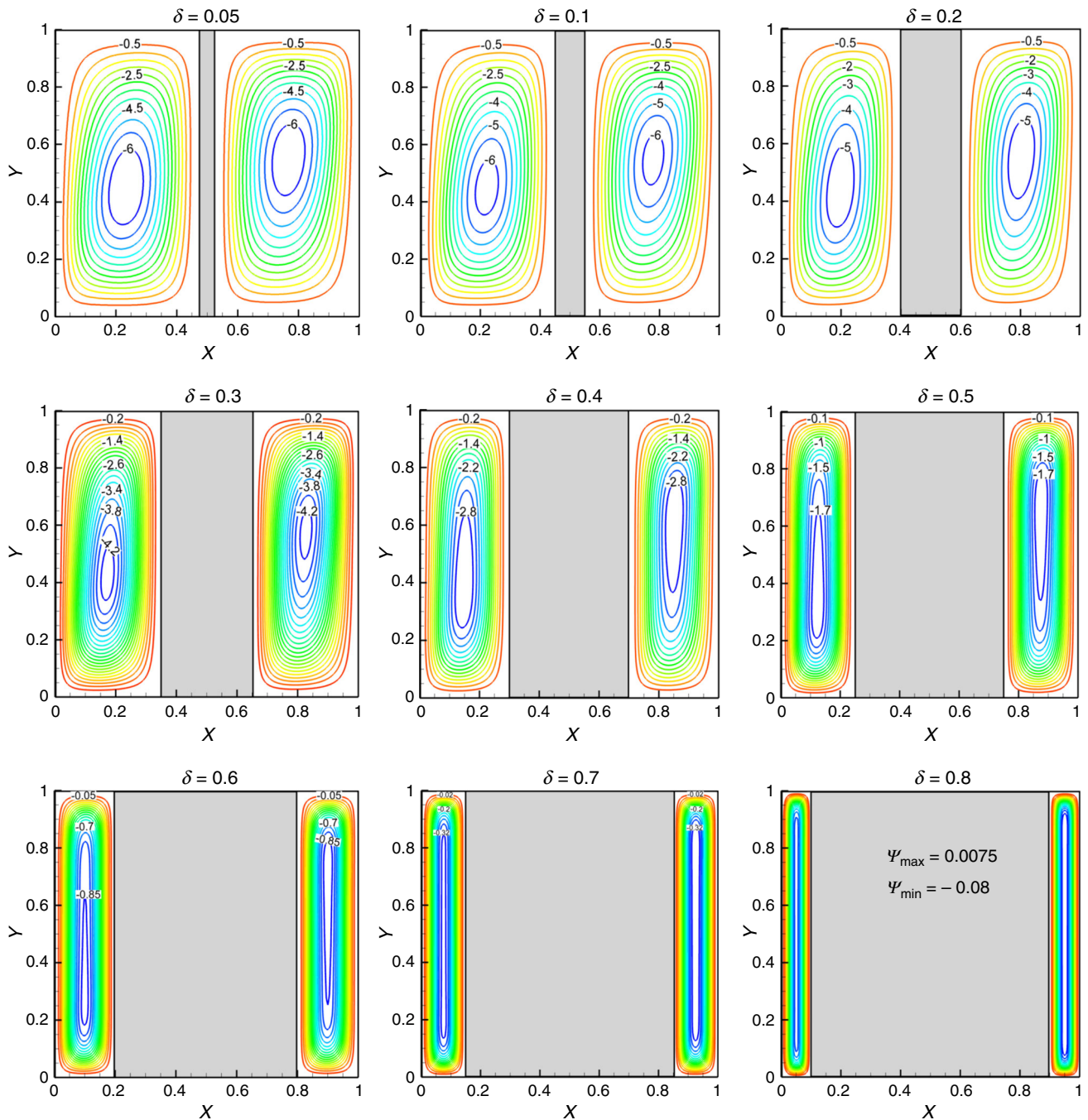

Fig. 6 Variation of the local Nusselt number in cases with and without partition for k_r=6.22, δ=0.1

Fig. 8 Streamlines at different partition thicknesses for $Ra = 10^5$, $k_r = 6.22$ and $X_s = 0.5$

temperature gradient is non-constant at low δ (nonlinear variation); however, it is visibly constant at high values of δ, leading to a linear variation of X-coordinates.

Figure 10 shows the temperature profiles $\theta(X, 0.5)$ presenting the transient evolution of the heat transfer in the domain. The temperature profiles present a centro-symmetric behavior ($X = 0.5$, $Y = 0.5$). By increasing the thickness δ, the temperature field follows a quasi-linear variation at mid-height and for high thickness values. This

behavior is more expressed at low δ values. The temperature profile follows a linear variation when δ rises toward 1. Besides, the temperature profile decreases linearly in the wall and in each part of the cavity for $\delta \geq 0.45$.

Figure 11 depicts the variation of the local Nusselt number at different partition thicknesses δ. It is shown that the local Nusselt number $Nu(y)$ on the active walls decreases with increasing vertical coordinate and with increasing partition thickness until a critical value is near
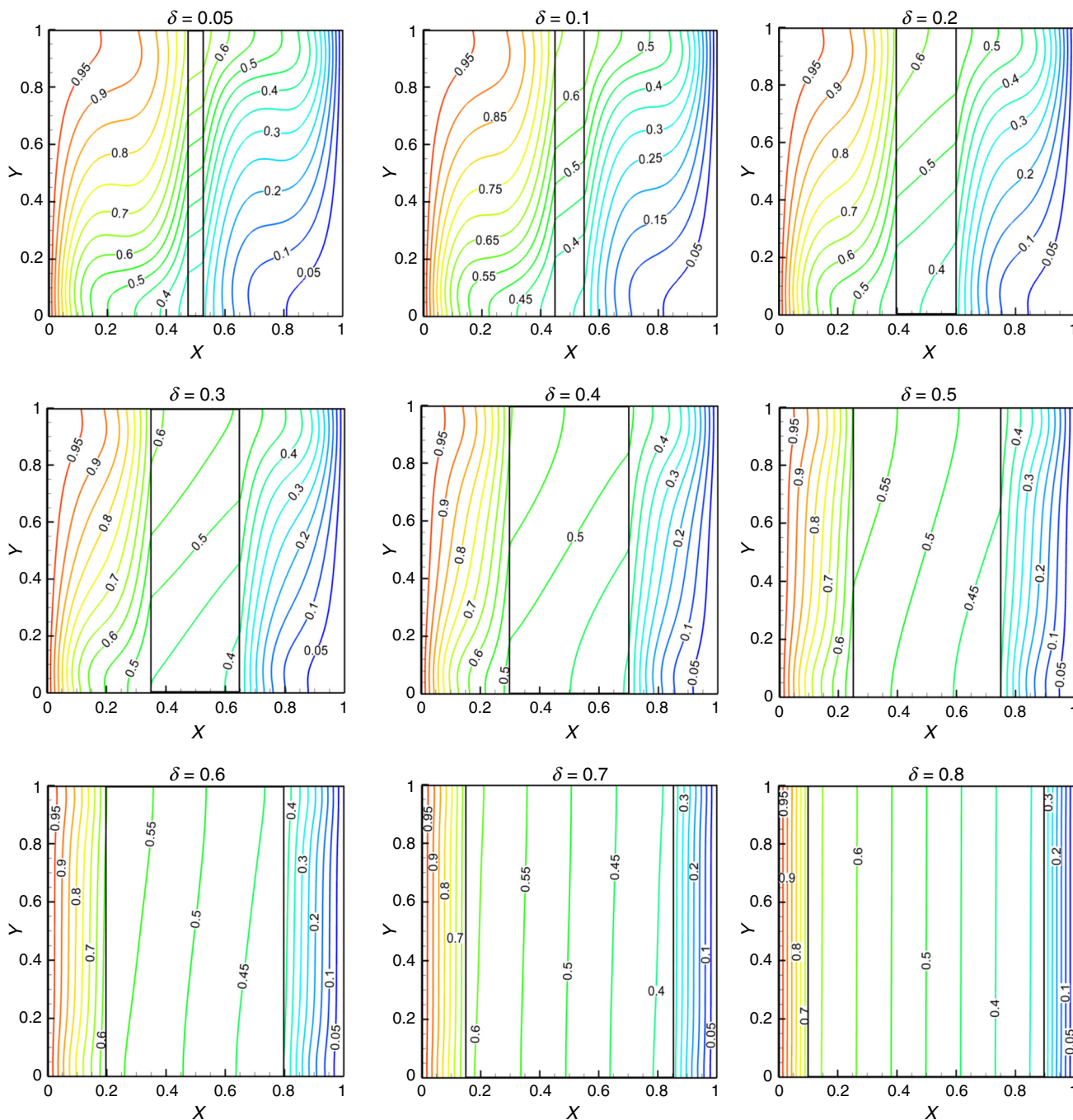
Fig. 9 Isotherms at different values of conducting body thickness for $Ra=10^5$, $k_r=6.22$ and $X_s=0.5$

0.5. This is attributed to the partition dumping effect of the convective current from the hot to the cold wall. Since $\delta \approx$ 0.5, as the wall thickness increases, the variation of the local Nusselt number becomes constant. The thermal communication is controlled by the conduction-dominant mode between the hot and cold walls which becomes more enhanced. This will increase the degree of heating and cooling on both walls.

Figure 12 shows the variation of the LB average Nusselt number at different wall thicknesses compared with the FE results obtained by COMSOL. A good agreement can be observed for the values obtained by the two approaches. A change in the isotherms (in temperature gradients) is noted. Such an effect has an impact on the average Nusselt number, which tends to decrease with the increase in the thickness of the wall. The partition exerts a lower driving
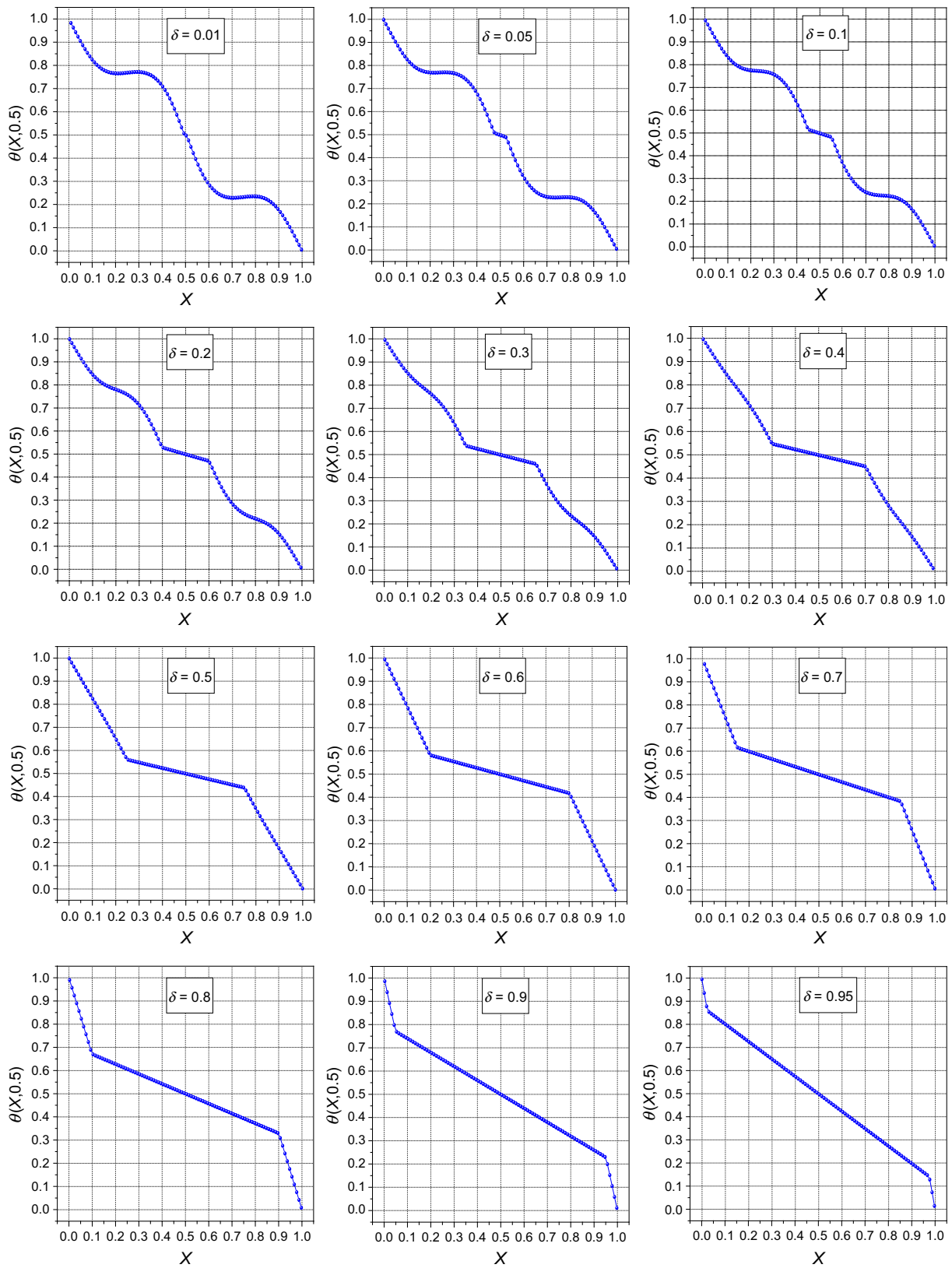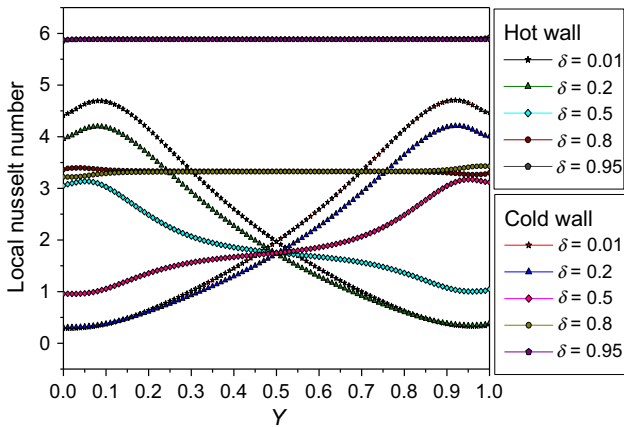
Fig. 10 Temperature profile θ(X, 0.5) at different values of conducting body thickness for $Ra=10^5$, $k_r=6.22$ and $X_s=0.5$

Fig. 11 Variation of the local Nusselt number at different partition thicknesses for $Ra=10^5$, $k_r=6.22$ and $X_s=0.5$

force on each part of the enclosure and thus reduces the heat transfer for $\delta \leq 0.45$.

By increasing the thickness of the wall ($\delta \geq 0.45$), the distance between the partition and the active walls decreases to favor the confinement, which leads to an increased heat exchange with the partition. In addition, we observe an increase in the mean Nusselt number for $\delta \geq 0.5$. The convective currents become much accelerated. In addition, the rotational movement of the fluid adjacent to the hot and cold active walls improves the heat transfer through the enclosure.

Figure 13 shows the flow structure at different positions of the wall partition from the cavity for different Rayleigh numbers. It may be observed that by decreasing the distance between the partition and the hot wall at $Ra=10^3$ and 10^4 a convective recirculation is formed in the big zone of the cavity. By increasing more the Ra number, we notice

the formation of a convective small recirculation in the small zone of the cavity. This behavior is observed for $X_s=$ 0.25 and $X_s=0.75$. For $Ra=10^6$ ($X_s=0.25$ and 0.75), we notice the development of the flow and the formation of two convective recirculation in the big zone of the cavity. The flow becomes unstable.

Effect of partition position and Rayleigh number

For $X_s=0.5$, a formation of two symmetrical circular structures is marked. The strength of these recirculations is weakened by increasing the Ra number. For instance at $X_s=0.25$, $\psi_{min}=-0.545$, -3.397 and -8.071 for, respectively, $Ra=10^3$, 10^4 and 10^5.

Figure 14 shows a succession of the isotherms contours at different positions of the conducting body for different Rayleigh numbers. The isotherms confirm the behavior of the flow structure. The isotherms are parallel near the smaller zone leading to a decrease in temperature gradient in this zone. With increasing Ra number, the heat transfer mechanism varies from conduction-dominant regime to convection-dominant regime.

By analyzing the temperature profile at different positions of the wall partition and different Ra numbers (Fig. 15), the temperature decreases in the small zone of the cavity for $X_s=0.25$ and $X_s=0.75$ according to an affine line with a slope greater than that of the temperature in the solid conductor. For $X_s=0.25$, the temperature presents a symmetrical character at mid-height and its profile is centro-symmetric of center ($X=0.5$, $Y=0.5$). At low Rayleigh numbers, the temperature decreases linearly. By increasing more the Rayleigh number, the temperature profile keeps the symmetrical character; however, it decreases linearly.
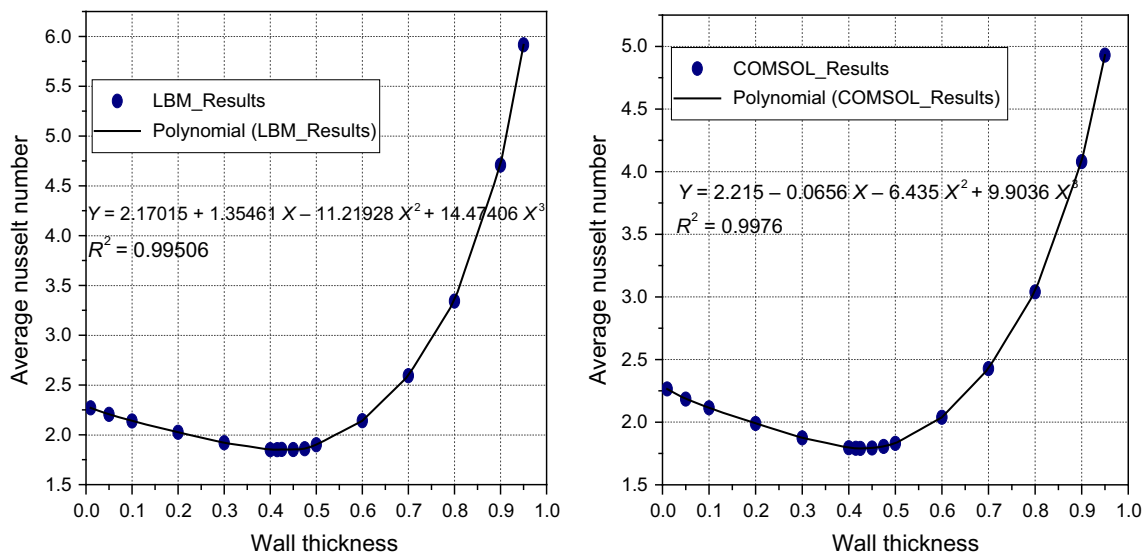

Fig. 12 Average Nusselt number versus partition thickness for $Ra=10^5$, $k_r=6.22$ and $X_s=0.5$
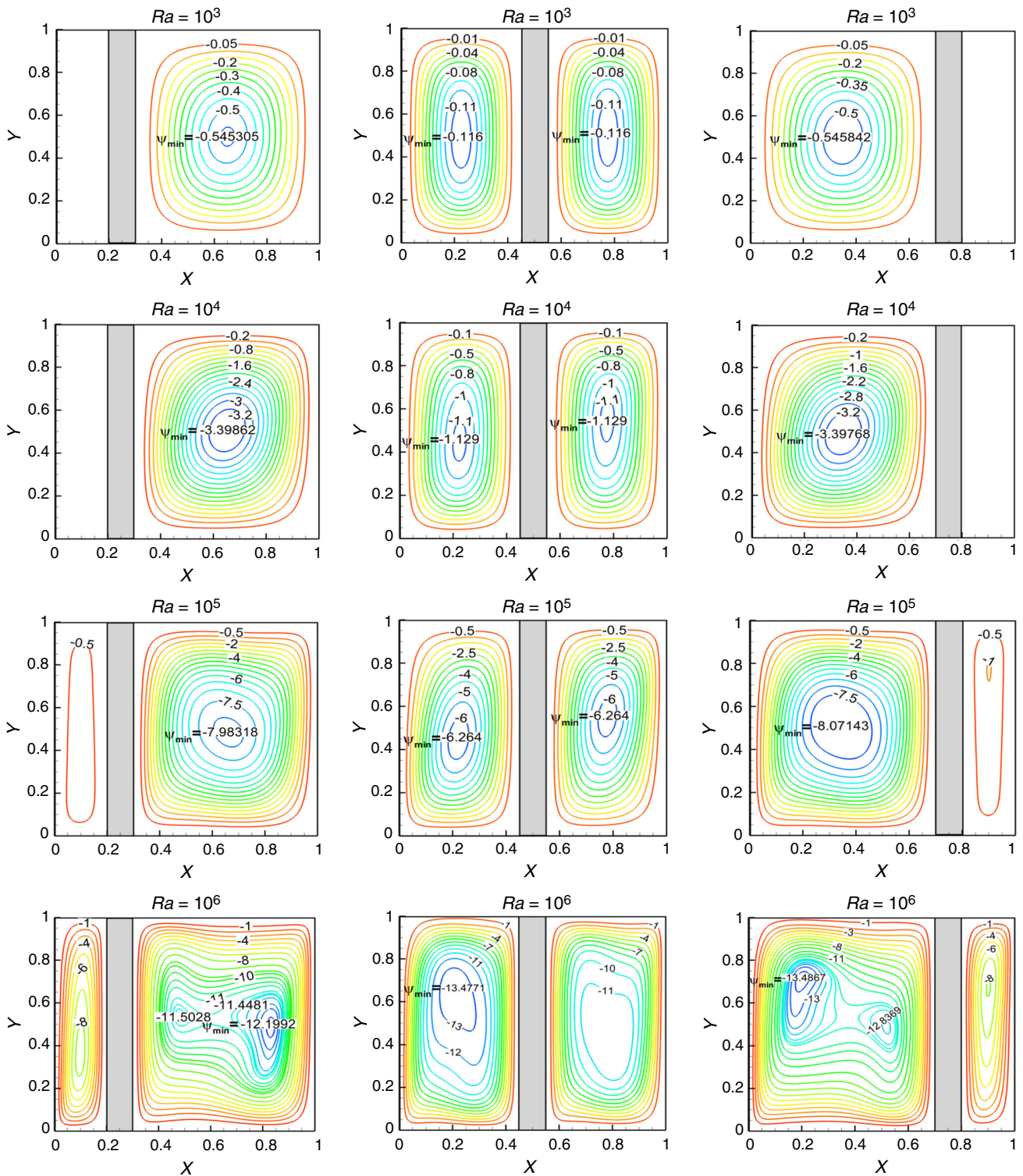
Fig. 13 Streamlines at different positions of conducting body: (left) $X_s=0.25$, (middle) $X_s=0.5$, (right) $X_s=0.75$, for different Ra numbers, $k_r=6.22$ and $\delta=0.1$

In Fig. 16, the local Nusselt number takes higher values in the leading edge of the hot surface ($X = 0$) and decreases by increasing the vertical coordinate Y. For $X_s = 0.25$, the local Nusselt number follows a symmetric behavior; this is explained by the symmetrical character of the convective flow. For $X_s = 0.25$, the heat transfer is more important at the cold wall than at the hot wall; indeed, the local Nusselt number at the cold wall is greater than that at the hot wall. At $Ra = 10^6$, the local
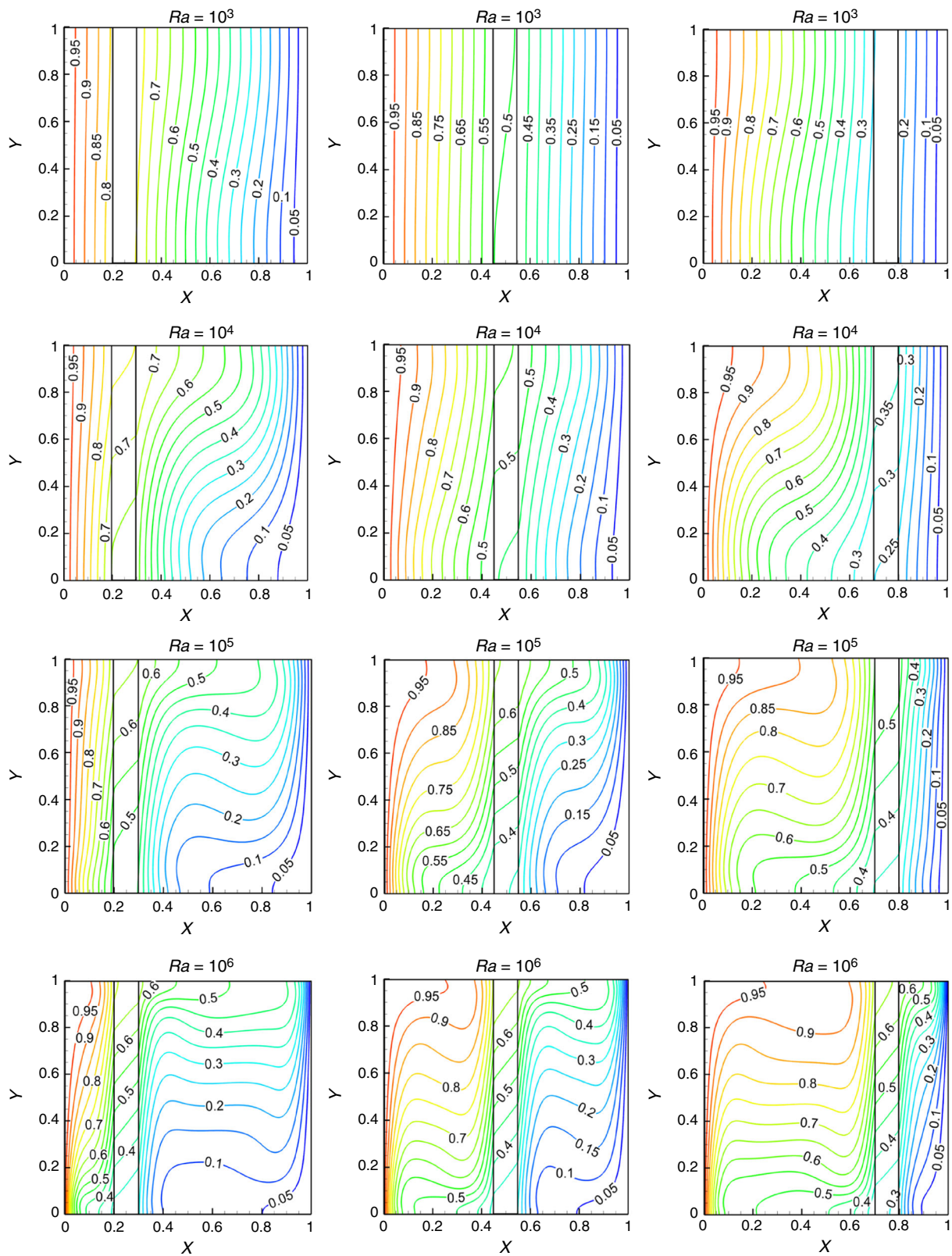
Fig. 14 Isotherms at different positions of partition: (left) $X_s=0.25$, (middle) $X_s=0.5$, (right) $X_s=0.75$, for different Ra numbers, $k_r=6.22$ and $\delta=0.1$
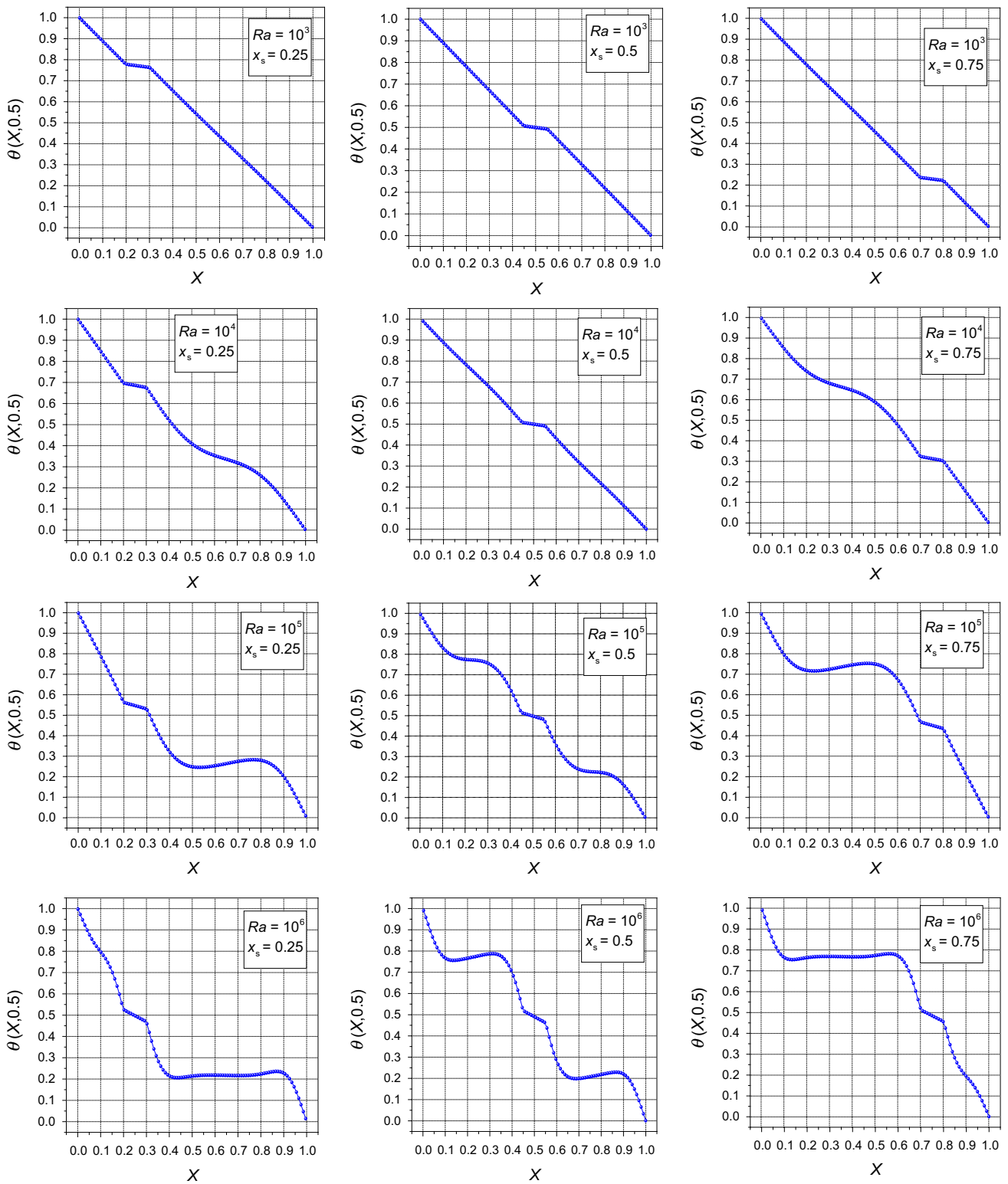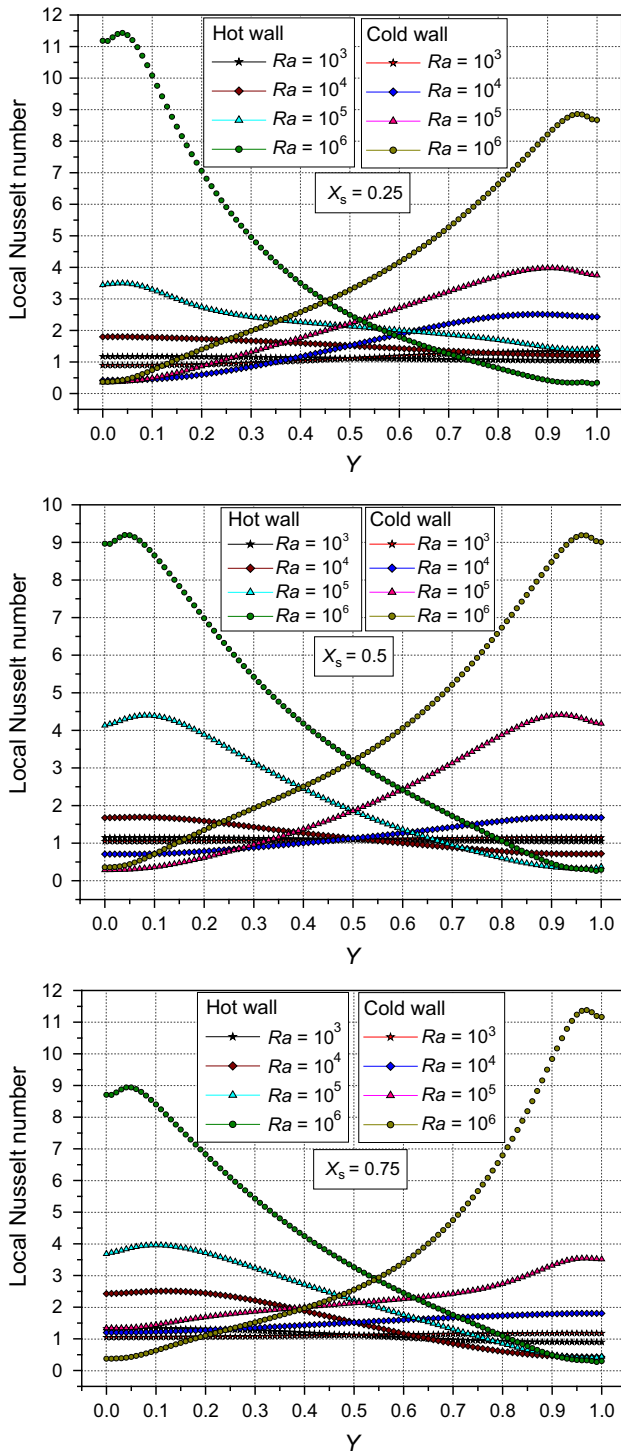
Fig. 15 Temperature profile at different positions of partition: (left) X_s=0.25, (middle) X_s=0.5, (right) X_s=0.75, for different Ra numbers, k_r= 6.22 and δ=0.1
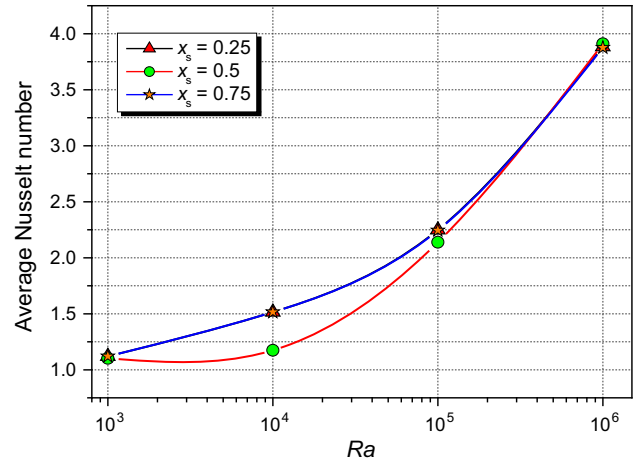
Nusselt number is more important at the hot wall, this is due to the interaction between the two structures, and this last increases the local heat transfer. For $X_s = 0.75$, the local Nusselt number becomes more important at the hot wall execpted $Ra = 10^6$ the local Nusselt number becomes greater at the cold wall. This behavior is due to the unsteadiness. In addition, with

Fig. 17 Variation of the average Nusselt number as a function of Rayleigh number at different positions of the wall for k_r=6.22 and δ= 0.1

Figure 17 presents the variation of the average Nusselt number at different positions of the conducting solid for different Rayleigh numbers. The average Nusselt number increases with the partition. This is noticed for Ra=10^4 and Ra=10^5. For Ra=10^3 and Ra=10^6, the average Nusselt number is the same. Besides, the average Nusselt number increases with increasing Rayleigh number. The average Nusselt numbers at X_s=0.25 and X_s=0.75 are the same due to symmetry.

The effect of partition position on the average Nusselt number is shown in Fig. 18 for different values of X_s for Ra= 10^5 and Ra=10^6. For Ra=10^5, the heat transfer rate decreases with the partition position until a critical value close to 0.325 and rises slightly until X_s=0.5. The critical position value decreases with the increase in Ra number and it is close to 0.2 for Ra=10^6 where Nu=3.766. For $X_s \geq 0.325$, the average Nusselt number remains almost constant, indicating a negligible effect. This observed effect of the partition position was also reported by Khatamifar et al. [22] for $0.25 \leq X_s \leq 0.75$ and Kahveci [53] where it has been found that the effect of the body position on the average Nusselt number is very weak.

Effect of thermal conductivity ratio

Figure 19 shows the flow structure at different thermal conductivity ratios and different Rayleigh numbers. The variation of thermal conductivity has not an effect on the flow structure. The flow is unicellular on either sides of the partition, and diagonal symmetric streamlines are almost identical. By observing the values of the stream function, the flow keeps its symmetrical behavior.

The isotherms at different thermal conductivity ratios are presented in Fig. 20. The contours of temperature are parallel at low values of k_r and Ra. The heat transfer across the air cavities is evidently conductive dominated, as
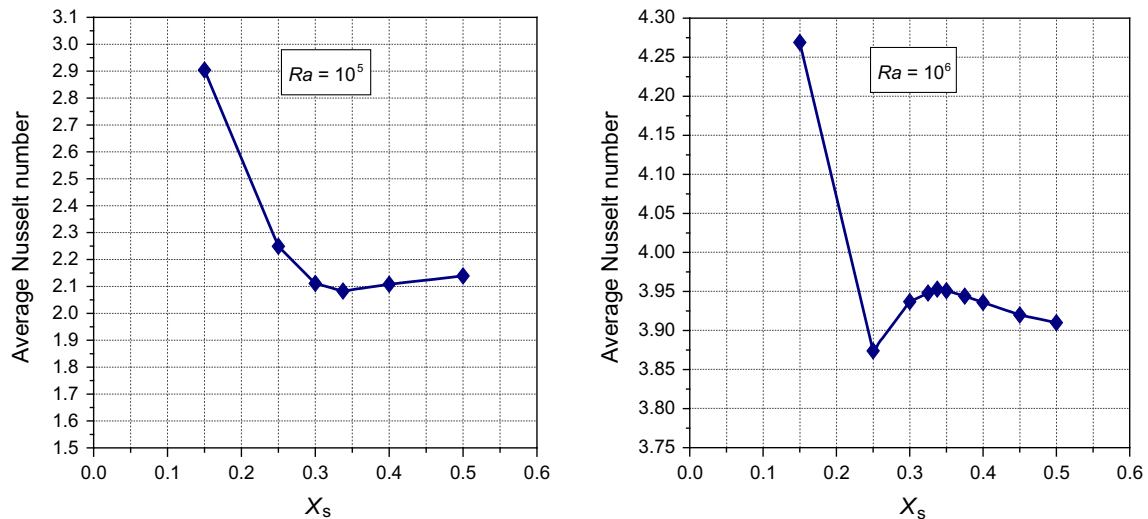
Fig. 16 Local Nusselt number variation at hot and cold walls for different Rayleigh numbers and different positions for k_r=6.22 and δ =0.1

decreasing partition position, the local Nusselt number increases. For instance, for X_s = 0.75 at Y = 0, the Nu_{avg} is close to 11; the same is for X_s = 0.75. Besides, the Nusselt number increases with increasing Rayleigh number.

Fig. 18 Variation of the average Nusselt number as a function of the wall position for k_r=6.22 and δ=0.1

indicated by the uniformly distributed isotherms. By increasing the thermal conductivity ratio, the isotherms become vertical in the partition region. The existence of plateaus in the core regions may be observed. The isotherms in the cavity with CHT appear to be increasingly deformed and crowded into the vicinity of the solid wall.

The average heat transfer rate across the cavity with CHT is the primary quantity of practical interest in this study. Figure 21 presents the variation of the average Nusselt number with the thermal conductivity ratio at different Rayleigh numbers. It can be found that for low Rayleigh numbers the heat transfer rate appears to be slightly affected by the increase in thermal conductivity ratio. For $Ra=10^3$ and $Ra=10^4$, the heat transfer rate is less affected by varying the thermal conductivity ratio. For $Ra=10^5$ and $Ra=10^6$, the average Nusselt number increases for $k_r<6.22$ and converges to constant value for high k_r values.

Heat transfer correlation

Several correlations are cited in the literature for the average Nusselt numbers for the two following cases:

- *Non-partitioned enclosure* Karayiannis et al. [54] give a correlations as follows:

$$\overline{Nu} = 0.155 Ra^{0.29} \quad \text{for} \quad A_r = \frac{H}{W} = 1 \tag{33}$$

$$\overline{Nu} = 0.247 A_r^{-0.20} Ra^{0.26} \quad \text{for} \quad 2 \le A_r = \frac{H}{W} \le 10 \tag{34}$$

The present study is concerned with the case A_r=1.

- *Cavity with conjugate heat transfer* For this case, many correlations are proposed. For instance, the correlation proposed by Duxbury [55]:

$$\overline{Nu} = 0.339 A_r^{-0.25} Ra^{0.25} (N+1)^{-1.25} \tag{35}$$

where N is the number of partitions inside the cavity.

Nishimura et al. [56] proposed a similar correlation, but he assumed a thin partition in the cavity.

$$\overline{Nu} = 0.29 A_r^{-0.25} Ra^{0.25} (N+1)^{-1} \quad \text{For} \quad A_r = \frac{H}{W} \ge 1 \tag{36}$$
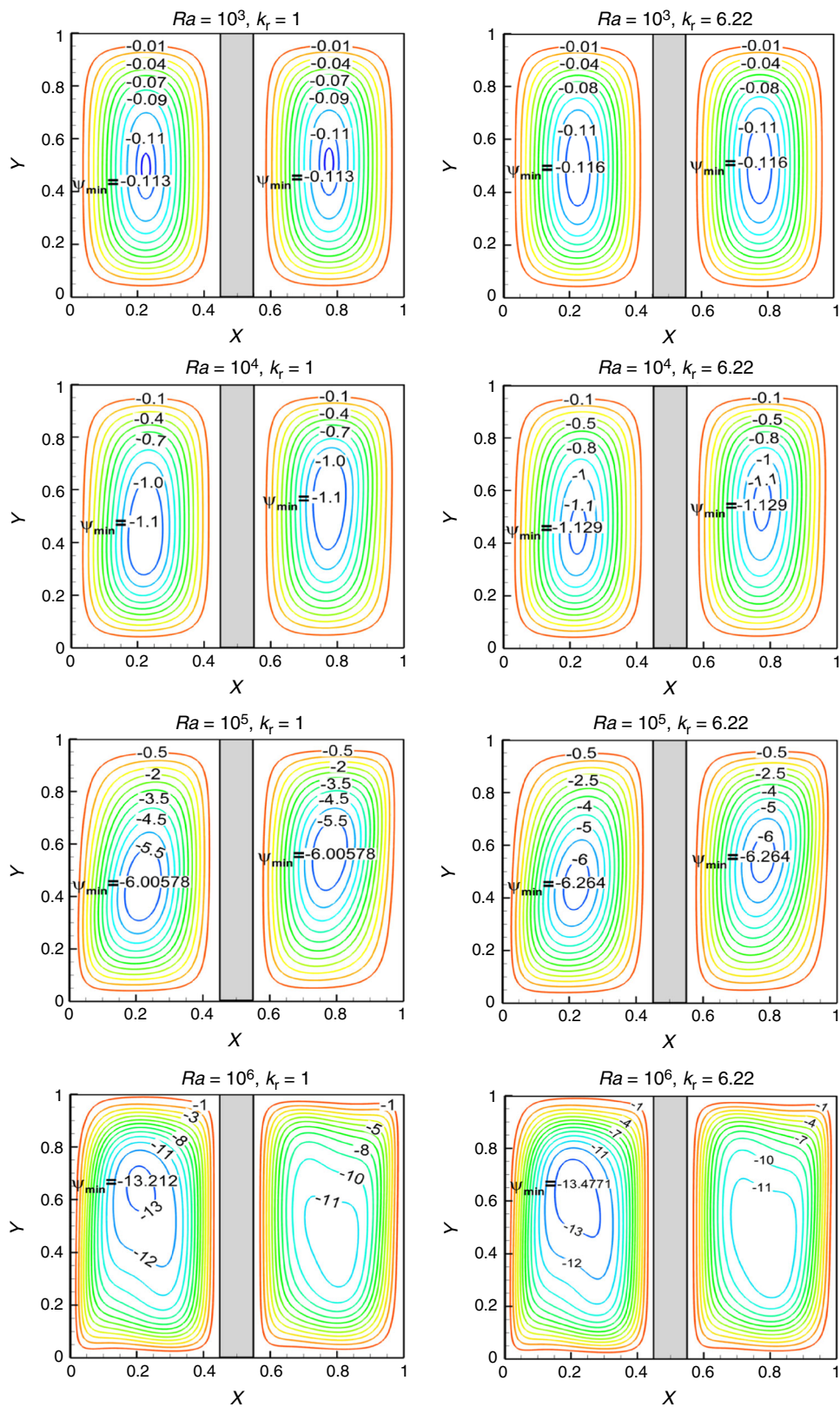
More recently, Souayeh et al. [27] developed the following correlation which incorporates the effect of Rayleigh number and the dimensionless conducting block location X_s.

$$\overline{Nu} = A(X_s) + B(X_s) \times Ra^{\frac{1}{2}} \tag{37}$$

Based on the correlation of Karayiannis et al. [55], the mean Nusselt number obtained from aforementioned correlation with the numerical results for a non-partitioned enclosure is presented in Fig. 22. It is clear that Nu increases with increasing Ra. This figure approves a linear dependency of the variation of the average Nusselt number. A good agreement is observed in the figure.

For the case of an enclosure with CHT and based on correlation of Duxbury [55] and Nishimura et al. [56], the comparison of the empirical correlation with the numerical average Nusselt number is depicted in Fig. 23. From the figure, it is seen that the average Nusselt number increases linearly with the Rayleigh number.
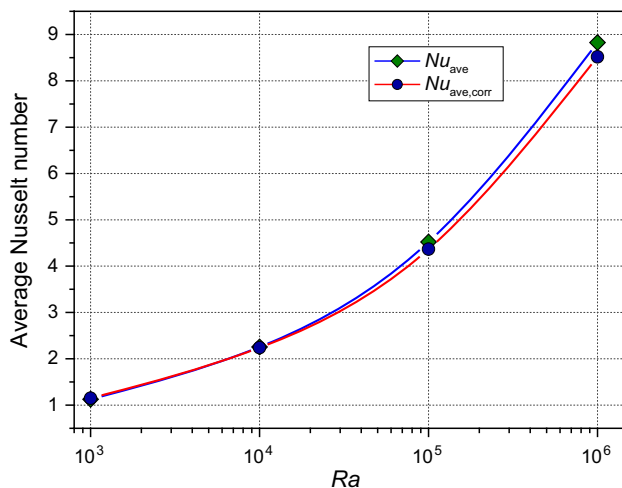
Fig. 20 Isotherms at different values of thermal conductivity and different Rayleigh numbers with X_s=0.5 and δ=0.1
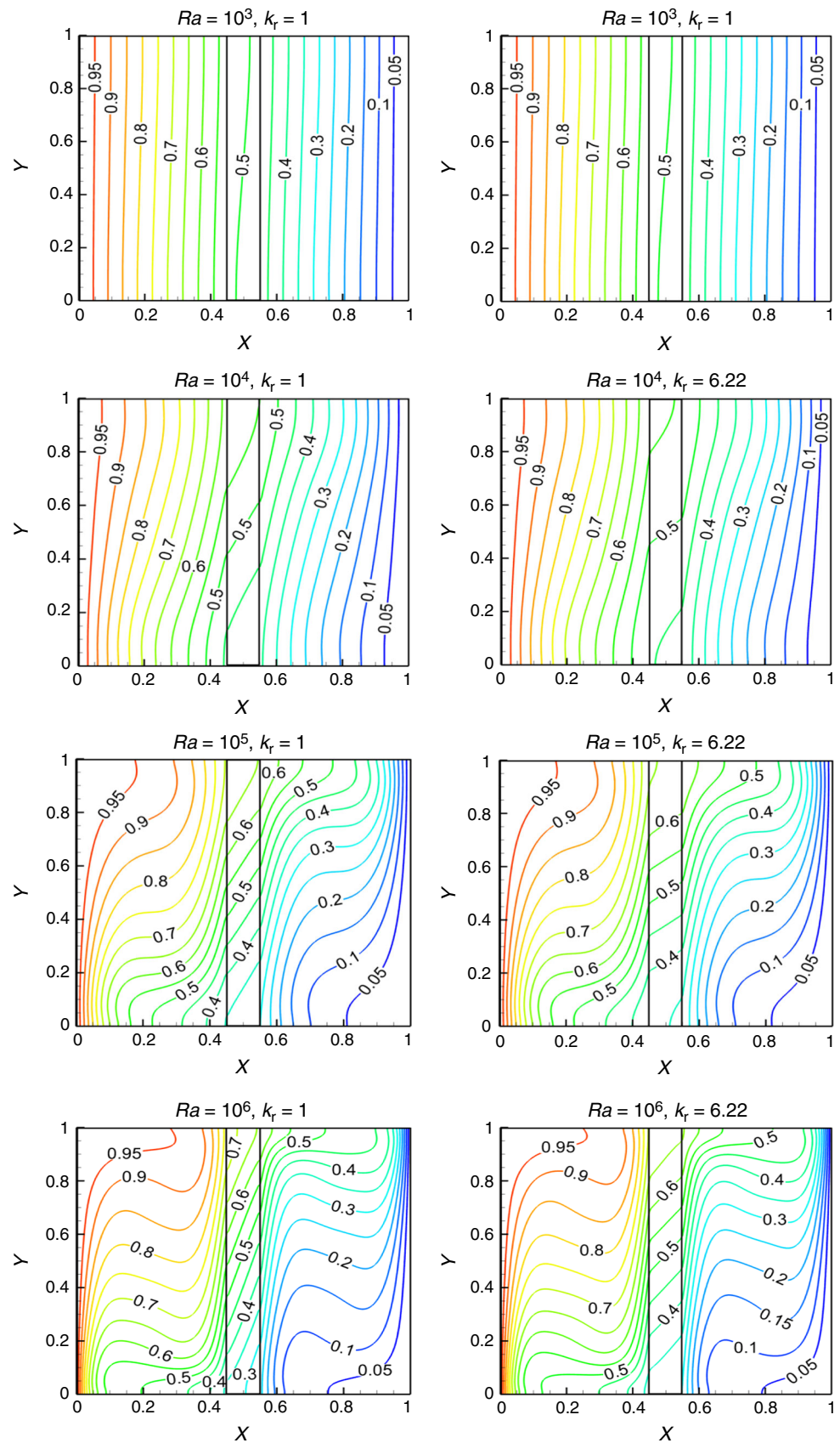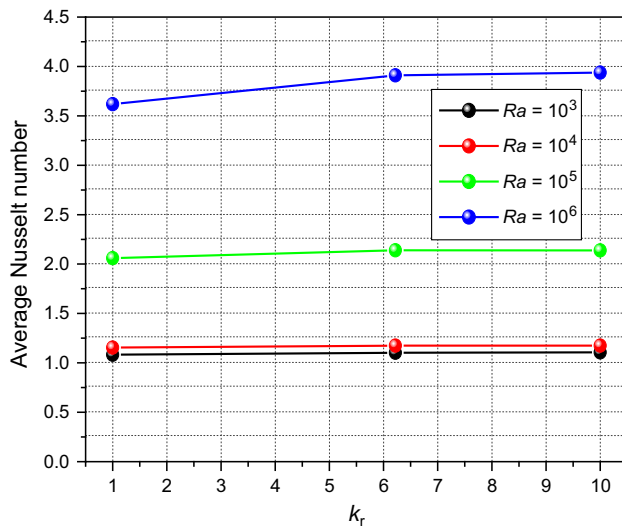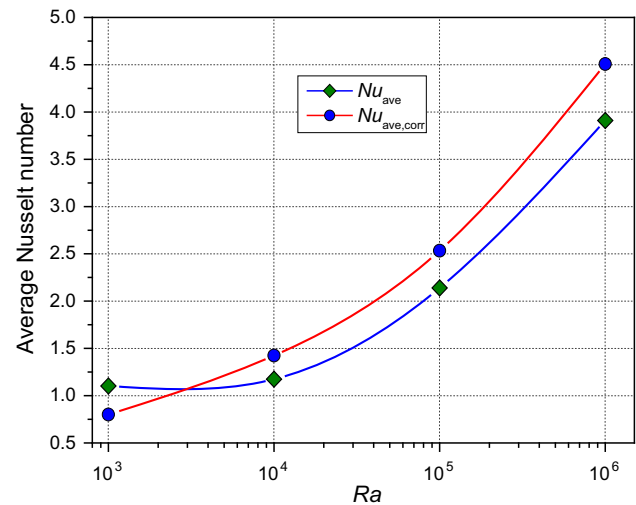
Fig. 21 Variation of the average Nusselt number at different values of thermal conductivity ratio for different Rayleigh numbers for X_s=0.5 and δ=0.1

Fig. 23 Variation of the numerical and correlated mean Nusselt number with Rayleigh number for a partitioned enclosure k_r=6.22, X_s =0.5 and δ=0.1

- The presence of partition in the cavity has a significant influence on the natural convection heat transfer characteristics.

- The rate of heat transfer decreases with increasing wall thickness for δ≤0.5. When δ tends toward 1, the average Nusselt number increases.

- The average Nusselt number is more affected by the position of the wall partition but is an increasing function of the Rayleigh number.

- The variation of thermal conductivity ratio increases the rate of heat transfer.

The mainly studied thermal conductivity ratio is k_r= 6.22. The air thermal conductivity at home temperature is close to 0.026. By multiplying the last value by 6.22, the solid thermal conductivity is close to 0.16. Such a value is characteristic of materials used in the building such as cellular concrete, wood, wood fiber-board and wood particle board, which presents a fallout of specific applications of partitioning of premises in the building.

Besides, it has been shown that the Lattice Boltzmann method is a powerful approach for investigating heat and fluid flow problems in multiphase media as well as for its simplicity of coding and its reasonable convergence CPU time in such stationary problems. In the following steps, MHD effects in microgeometries will be accounted for as an issue of important interest.

Fig. 22 Variation of the numerical and correlated mean Nusselt number with Rayleigh number for a non-partitioned enclosure k_r= 6.22, X_s=0.5 and δ=0.1

Conclusions

In this paper, a numerical investigation of natural CHT in a differentially heated cavity divided by a conducting solid has been performed using LBM. The numerical simulation is carried over a wide range of the Rayleigh number 10^3–10^6. The effects of wall thickness, the wall position and Rayleigh number as well as the effect of the thermal conductivity ratio are studied. The distribution of streamlines, isotherms, local and the averaged Nusselt number is used in order to understand the behavior of the flow and the mode of heat transfer. The main conclusions of this work can be summarized as follows:

References

1. Jajja SA, Ali W, Ali HM. Multiwalled carbon nanotube nanofluid for thermal management of high heat generating computer processor. Heat Transf Asian Res. 2014;43(7):653–66.

2. Jajja SA, Ali W, Ali HM, Ali AM. Water cooled minichannel heat sinks for microprocessor cooling: effect of fin spacing. Appl Therm Eng. 2014;64(1–2):76–82.

3. Siddiqui AM, Arshad W, Ali HM, Ali M, Nasir MA. Evaluation of nanofluids performance for simulated microprocessor. Therm Sci. 2017;21(5):2227–36.

4. Arshad W, Ali HM. Graphene nanoplatelets nanofluids thermal and hydrodynamic performance on integral fin heat sink. Int J Heat Mass Transf. 2017;107:995–1001.

5. Arshad W, Ali HM. Experimental investigation of heat transfer and pressure drop in a straight minichannel heat sink using TiO_2 nanofluid. Int J Heat Mass Transf. 2017;110:248–56.

6. Ali HM, Azhar MD, Saleem M, Saeed QS, Saieed A. Heat transfer enhancement of car radiator using aqua based magnesium oxide nanofluids. Therm Sci. 2015;19(6):2039–48.

7. Ali HM, Ali H, Liaquat H, Maqsood HTB, Nadir MA. Experimental investigation of convective heat transfer augmentation for car radiator using ZnO–water nanofluids. Energy. 2015;84(1):317–24.

8. Fiebig M, Grosse-Gorgemann A, Chen Y, Mitra N. Conjugate heat transfer of a finned tube part A: heat transfer behavior and occurrence of heat transfer reversal. Numer Heat Transf A Appl. 1995;28(2):133–46.

9. Nigen J, Amon C. Time-dependent conjugate heat transfer characteristics of self-sustained oscillatory flows in a grooved channel. J Fluids Eng. 1994;116(3):499–507.

10. Ha MY, Jung MJ. A numerical study on three-dimensional conjugate heat transfer of natural convection and conduction in a differentially heated cubic enclosure with a heat-generating cubic conducting body. Int J Heat Mass Transf. 2000;43(23):4229–48.

11. Patankar S (ed). A numerical method for conduction in composite materials, flow in irregular geometries and conjugate heat transfer. In: Proceedings 6th international heat transfer conference; 1978.

12. Juncu G. The influence of the physical properties ratios on the conjugate heat transfer from a drop. Heat Mass Transf. 1999;35(3):251–7.

13. Djebali R, Pateyron B, ElGanaoui M. A lattice Boltzmann-based study of plasma sprayed particles behaviours. Comput Mater Contin. 2011;25(2):159–75.

14. Djebali R, Ganaoui ME, Pateyron B. A lattice Boltzmann-based investigation of powder in-flight characteristics during APS process, part I: modelling and validation. Prog Comput Fluid Dyn. 2012;12(4):270–8.

15. Djebali R, Pateyron B, El Ganaoui MA. Lattice Boltzmann based investigation of powder in-flight characteristics during APS process, part II: effects of parameter dispersions at powder injection. Surf Coat Technol. 2013;220:157–63.

16. Djebali R. Investigating plasma jets behavior using axisymmetric lattice Boltzmann model under temperature dependent viscosity. Commun Comput Phys. 2014;15(3):677–91.

17. Lu J, Lei H, Dai C. A simple difference method for lattice Boltzmann algorithm to simulate conjugate heat transfer. Int J Heat Mass Transf. 2017;114:268–76.

18. Mohamad A, Tao Q, He Y, Bawazeer S. Treatment of transport at the interface between multilayers via the lattice Boltzmann method. Numer Heat Transf B Fundam. 2015;67(2):124–34.

19. Koca A, Oztop HF, Varol Y, Mobedi M. Using of Bejan's heatline technique for analysis of natural convection in a divided cavity with differentially changing conductive partition. Numer Heat Transf A Appl. 2013;64(4):339–59.

20. Karani H, Huber C. Lattice Boltzmann formulation for conjugate heat transfer in heterogeneous media. Phys Rev E. 2015;91(2):023304.

21. Benachour E, Draoui B, Imine B, Asnoune K. Numerical simulation of conjugate convection combined with the thermal conduction using a polynomial interpolation method. Adv Mech Eng. 2017;9(5):1–7.

22. Khatamifar M, Lin W, Armfield S, Holmes D, Kirkpatrick M. Conjugate natural convection heat transfer in a partitioned differentially-heated square cavity. Int Commun Heat Mass Transf. 2017;81:92–103.

23. Ho C, Yih Y. Conjugate natural convection heat transfer in an air-filled rectangular cavity. Int Commun Heat Mass Transf. 1987;14(1):91–100.

24. Saeid NH. Conjugate natural convection in a vertical porous layer sandwiched by finite thickness walls. Int Commun Heat Mass Transf. 2007;34(2):210–6.

25. Wang J, Wang M, Li Z. A lattice Boltzmann algorithm for fluid–solid conjugate heat transfer. Int J Therm Sci. 2007;46(3):228–34.

26. Seddiq M, Maerefat M, Mirzaei M. Modeling of heat transfer at the fluid–solid interface by lattice Boltzmann method. Int J Therm Sci. 2014;75:28–35.

27. Souayeh B, Ben-Cheikh N, Ben-Beya B. Effect of thermal conductivity ratio on flow features and convective heat transfer. Particul Sci Technol. 2017;35(5):565–74.

28. Ben-Nakhi A, Chamkha AJ. Effect of length and inclination of a thin fin on natural convection in a square enclosure. Numer Heat Transf. 2006;50(4):381–99.

29. Ben-Nakhi A, Chamkha AJ. Conjugate natural convection in a square enclosure with inclined thin fin of arbitrary length. Int J Therm Sci. 2007;46(5):467–78.

30. Ismael MA, Chamkha AJ. Conjugate natural convection in a differentially heated composite enclosure filled with a nanofluid. J Porous Media. 2015;18(7):699–716.

31. Chamkha AJ, Hussain SH, Abd-Amer QR. Mixed convection heat transfer of air inside a square vented cavity with a heated horizontal square cylinder. Numer Heat Transf A Appl. 2011;59(1):58–79.

32. Chamkha AJ, Ismael MA. Conjugate heat transfer in a porous cavity heated by a triangular thick wall. Numer Heat Transf A Appl. 2013;63(2):144–58.

33. Chamkha AJ, Ismael MA. Natural convection in differentially heated partially porous layered cavities filled with a nanofluid. Numer Heat Transf A Appl. 2014;65(11):1089–113.

34. Ismael MA, Armaghani T, Chamkha AJ. Conjugate heat transfer and entropy generation in a cavity filled with a nanofluid-saturated porous media and heated by a triangular solid. J Taiwan Inst Chem Eng. 2016;59:138–51.

35. Bhatnagar PL, Gross EP, Krook M. A model for collision processes in gases. I. Small amplitude processes in charged and neutral one-component systems. Phys Rev. 1954;94(3):511–25.

36. Djebali R, El Ganaoui M. Assessment and computational improvement of thermal lattice Boltzmann models based benchmark computations. Comput Model Eng Sci. 2011;71(3):179–202.

37. Djebali R, El Ganaoui M, Pateyron B, Sammouda H. Simulation and modeling of turbulent plasma jet based on axisymetric LBGK model. Defect Diffus Forum. 2011;312–315:1167–71.

38. Abbassi MA, Safaei MR, Djebali R, et al. LBM simulation of free convection in a nanofluid filled incinerator containing a hot block. Int J Mech Sci. 2018;144:172–85.

39. Djebali R, Elganaoui M, Jaouabi A, Pateyron B. Scrutiny of spray jet and impact characteristics under dispersion effects of powder injection parameters in APS process. Int J Therm Sci. 2016;100:229–39.

40. Djebali R, Abbassi MA, Jaouabi A. A lattice Boltzmann model for the simulation of flows and heat transfer at very high temperature: a dynamic framework of conversion to physical space with test cases. In: Driss Z, Necib B, Zhang HC, editors. Thermo-mechanics

applications and engineering technology. Cham: Springer; 2018. p. 151–69. https://doi.org/10.1007/978-3-319-70957-4_7.

41. Mohamad A, Kuzmin A. A critical evaluation of force term in lattice Boltzmann method, natural convection problem. Int J Heat Mass Transf. 2010;53(5–6):990–6.

42. Bairi A. Nusselt–Rayleigh correlations for design of industrial elements: experimental and numerical investigation of natural convection in tilted square air filled enclosures. Energy Convers Manag. 2008;49(4):771–82.

43. Djebali R, El Ganaoui M, Sammouda H. Investigation of a side wall heated cavity by using lattice Boltzmann method. Eur J Comput Mech/Revue Européenne de Mécanique Numérique. 2009;18(2):217–38.

44. Dixit H, Babu V. Simulation of high Rayleigh number natural convection in a square cavity using the lattice Boltzmann method. Int J Heat Mass Transf. 2006;49(3–4):727–39.

45. Kuznik F, Vareilles J, Rusaouen G, Krauss G. A double-population lattice Boltzmann method with non-uniform mesh for the simulation of natural convection in a square cavity. Int J Heat Fluid Flow. 2007;28(5):862–70.

46. Moumni H, Welhezi H, Djebali R, Sediki E. Accurate finite volume investigation of nanofluid mixed convection in two-sided lid driven cavity including discrete heat sources. Appl Math Model. 2015;39(14):4164–79.

47. Hortmann M, Perić M, Scheuerer G. Finite volume multigrid prediction of laminar natural convection: benchmark solutions. Int J Numer Meth Fluids. 1990;11(2):189–207.

48. de Vahl Davis G. Natural convection of air in a square cavity: a bench mark numerical solution. Int J Numer Methods Fluids. 1983;3(3):249–64.

49. Khanafer K, Vafai K, Lightstone M. Buoyancy-driven heat transfer enhancement in a two-dimensional enclosure utilizing nanofluids. Int J Heat Mass Transf. 2003;46(19):3639–53.

50. Mobedi M. Conjugate natural convection in a square cavity with finite thickness horizontal walls. Int Commun Heat Mass Transf. 2008;35(4):503–13.

51. Kalita JC, Dalal D, Dass AK. Fully compact higher-order computation of steady-state natural convection in a square cavity. Phys Rev E. 2001;64(6):1–13.

52. COMSOL Multiphysics Reference Manual, version 4.3, COMSOL, Inc, www.comsol.com.

53. Kahveci K. Buoyancy driven heat transfer of nanofluids in a tilted enclosure. J Heat Transf. 2010;132(6):1–12.

54. Karayiannis T, Ciofalo M, Barbaro G. On natural convection in a single and two zone rectangular enclosure. Int J Heat Mass Transf. 1992;35(7):1645–57.

55. Duxbury D. An interferometric study of natural convection in enclosed plane air layers with complete and partial central vertical divisions: University of Salford; 1979.

56. Nishimura T, Shiraishi M, Nagasawa F, Kawamura Y. Natural convection heat transfer in enclosures with multiple vertical partitions. Int J Heat Mass Transf. 1988;31(8):1679–86.

Publisher's Note

Springer Nature remains neutral with regard to jurisdictional claims in published maps and institutional affiliations.